ECN

Energy research Centre of the Netherlands

Analysis of aerodynamic measurements on a model wind turbine placed in the NASA-Ames tunnel

ECN's and TUD's contribution to IEA Wind Task XX

J.G. Schepers (ECN)

R.P.J.O.M. van Rooij (TU Delft)

ECN-E--08-052

TU Delft

Delft University of Technology

Acknowledgement/Preface
Financial support for this research was given in part by SenterNovem, Project: 'IEA Annex XX: Analysis of NASA-Ames wind tunnel measurements'
Project Reference: 2020-02-11-10-005. ECN project number: 74189.

The present project could not be performed without the supply of data by the National Renewable Energy Laboratory, NREL in the USA, where in particular the support from Scott Schreck is highly appreciated.

Abstract
In this report the most important contributions of ECN and DUT to IEA Wind Task XX are summarized. IEA Wind Task XX is an international cooperation between several parties from 7 countries coordinated by the National Renewable Energy Laboratory, NREL from the USA.
The main aim of IEA Wind Task XX is to analyze the detailed aerodynamic measurements which were performed by NREL on a wind turbine placed in the large (24.4 x 36.6 m) NASA-Ames wind tunnel.

Contents

List of tables

List of figures

Summary

In this report the most important contributions of ECN and DUT to IEA Wind Task XX are summarized. IEA Wind Task XX is an international cooperation between several parties from 7 countries, coordinated by the National Renewable Energy Laboratory, NREL from the USA.
The main aim of IEA Wind Task XX is to analyze the measurements which were performed by NREL on a wind turbine placed in the large (24.4x36.6m) NASA-Ames wind tunnel.
This wind turbine was 2-bladed and it had a rotor diameter of 10 meter. One of the blades was instrumented with pressure taps at 5 radial positions to measure the local pressure distribution and the resulting sectional aerodynamic loads.
A large number of measurements at very different conditions were stored into a database and were made accessible to the IEA Wind Task XX participants.
The ECN contribution to Annex XX focused on a comparison of calculated results from ECN's aeroelastic code PHATAS (Lindenburg, 2005) and the free wake lifting line code AWSM (van Garrel, 2003) with measurements at non-yawed conditions, yawed conditions and at fast pitching steps (dynamic inflow). Furthermore a new model has been developed which covers instationary effects at attached flow conditions. Most comparisons between calculations and measurements are based on dimensional aerodynamic loads by which the uncertainty in dynamic pressure and angle of attack, which often complicates the interpretation of aerodynamic wind turbine measurements, does not play a role. It is noted that the description of ECN's activities in the present report is (almost) similar to the description which has been provided for the final report of IEA Wind Task XX.
The DUT contributions focused on the quality of the measurements and its repeatability. A thorough investigation into the parameters as wind speed, mis-alignment, blade pitch stability in relation to the flow behavior have been studied. And it turned out that a steady inflow condition does not mean a steady flow over the blade. It varies in span and chord wise direction. Apart from the flow behavior there was special interest in derivation of the local angle-of-attack. A proper inflow angle plays a key role in comparison of the characteristics between the segments but also between other blades. A simple adjustment of the measured flow probe angle is proposed but also a more comprehensive methodology has been derived with help of a free vortex wake model. In particular in the stalled and yawed conditions this method could be of great value and is of great interest if flow probes are not available like the recent measurements performed by the "Mexico" partners (EU project) in the DNW.
The second focus was at prediction methods for the segment airfoil characteristics along the blade span. The tuning parameters in general engineering methods (based on 2D performances) have been investigated and the earlier NREL field tests were included to analyze blade geometry effects. The same methods were compared with the most sophisticated aerodynamic approaches which contain a more detailed description of the flow ranging from boundary layer description to a full characterization of the flow field. Implementation of the aerodynamic properties in more detail showed far better results than the well known (simple) engineering models. The cur-rent report could be more elaborate then the final report of IEA Wind Task XX and is now a compilation of the expert meetings, conference papers and journals.

1. Introduction and goal

In this report the most important results of ECN's and DUT's contribution to IEA Wind Task XX are summarized. IEA Wind Task XX is an international cooperation between several parties from 7 countries, coordinated by the National Renewable Energy Laboratory, NREL from the USA. The Dutch Contribution to IEA Wind Task XX was sponsored by SenterNovem.
The project was carried out in the period from 2003-2007.

The main aim of IEA Wind Task XX was to analyze the measurements which were performed by NREL on a wind turbine placed in the large (24.4x36.6m) NASA-Ames wind tunnel.
This wind turbine was 2-bladed and it had a rotor diameter of 10 meter. One of the blades was instrumented with pressure taps at 5 radial positions to measure the local pressure distribution and the resulting sectional aerodynamic loads. A large number of measurements at very different conditions were stored into a database and made accessible to the IEA Wind Task XX participants.
The present set of measurements offers a unique base for the investigation of aerodynamic effects and for the validation and improvement of wind turbine design codes. An important advantage lies in the fact that aerodynamic forces are measured at different radial positions, by which local aerodynamic effects can be assessed. Usually wind turbine measurements only provide integrated blade and rotor loads which hide the details on sectional level.
As a matter of fact, local aerodynamic loads were also measured in IEA Annex XVIII, (Schepers et. al., 2002) but these measurements were taken on turbines in the free atmosphere, where the uncertainty due to the instationary, inhomogeneous and uncontrolled wind conditions formed an important problem (as it is in all field measurements). Hence a very important additional advantage of the present measurements lies in the wind tunnel environment, which yields (almost) stationary and homogeneous conditions. The huge size of the wind tunnel allows a rotor diameter of 10 m, with very little blockage effects. Obviously this rotor diameter is still (much) smaller than the diameter of the nowadays commercial wind turbines, but nevertheless the blade Reynolds number (in the order of 1 Million) is sufficiently high to make the aerodynamic phenomena at least to some extent representative for modern wind turbines.

In the ECN contribution to Annex XX, particular emphasis has been put on the validation of an aero-elastic code PHATAS (Lindenburg, 2005) and a free wake lifting line model AWSM (van Garrel, 2003). Special attention was paid to 1) non-yawed conditions, 2) yawed conditions and 3) dynamic inflow at fast pitching steps. The background/motivation to work on these conditions was as follows:

- From the comparison at non-yawed flow and relatively low tunnel speeds, the 'basic' accuracy of design codes at normal conditions could be assessed. The results at high tunnel speeds offered useful insights on 3D stall effects.
- The study on yawed conditions offered insight into the load variations which result from two effects:
  - The variation in induced velocity due to the skewed (asymmetric) wake geometry.
  - The advancing and retreating blade effect in combination with dynamic stall effects.
- Both effects determine the cyclic load fluctuation (which is relevant for fatigue load calculations). The first effect also contributes to the yawing stability. The variation of the induced velocity obviously mainly plays a role at high axial induction factors (i.e. relatively low wind speeds) where the advancing and retreating blade effect is in particular important at high tunnel speeds, which due to the large angle of attack, may lead to strong dynamic stall effects.
- The results at fast pitching transients offer insight into the dynamic inflow phenomenon. Dynamic inflow is characterized by an overshoot in loads followed by a gradual approach of the loads towards the new equilibrium value. These effects have a large practical importance, not

only in view of the higher dynamic loads on a turbine but also be-cause of its impact on the aerodynamic damping characteristics and in particular in the design of pitch control algorithms, see van Engelen and van ‘t Hooft (2004).

Finally ECN developed a model for the prediction of instationary effects at attached flow. These effects are important for the correct prediction of the stability of edgewise vibrations at pitching actions.

DUT’s main interest in this IEA Annex 20 is twofold: first is to investigate the flow behavior around the rotor blade and its corresponding loads and secondly to validate numerical approximations of blade and rotor loads with the aim to improve general engineering stall-models.
The first approach starts with carefully unraveling the characteristics to understand the flow behavior. For this purpose the non-yawed steady state is used and possible affecting parameters are addressed ranging from wind speed stability to rotor blade behavior. The attached flow could therefore serve as reference because flow variations are expected to be followed nicely. The derivation of the angle-of-attack from the flow probe measurements could be checked here and probe mis-alignment and correction methods can be evaluated. Results from earlier projects where correction methods have been evaluated on a 2D airfoil in the wind tunnel were of great help in the determination here. The obtained characteristics gives insight in aero-elastic behavior and shows dependencies in the rotor configuration (rpm, pitch angle and rotor plane part), blade geometry (chord and twist distribution) and airfoil characteristics. The non as-well as rotating configurations are investigated by Delft.
The second part of the investigation is into prediction of the blade segment performances in the non-rotating as-well as rotating configuration in the non-yawed conditions. The first configuration serves as reference for adjustment of finiteness of the blade, the so called wing corrections. But also gives insight in the parked load case which is still required for certification. The results found here could serve as guideline for bodies like Germanischer Lloyd or DNV.
The rotating configuration has been under subject by many and prediction of the segment performances to determine the blade loads is still unresolved. Most common are the approaches with (simple) engineering codes which use 2D measurements as base-line. Tuning parameters are then the key to model in particular augmented lift due to rotation. Additional corrections for unsteady inflow conditions, yawed flow etcetera have been implemented and wide variations for specific conditions have been derived. Here the focus is only on the span-wise distribution of the non-yawed and different geometries have been evaluated. The latter should at least confirm what should be required with taper and twist. In addition more sophisticated aerodynamic codes were applied to check engineering models and to figure out which relations could be added. Validation with a full Navier-Stokes code, like FLUENT, was not foreseen at the start of the project but improvements of these codes and strong increase in computer power to reduce calculation time make these codes accessible for the wind turbine industry. This becomes more and more coming practice. Applying the commercial code FLUENT is still not easy and requires quite some experience but the quality of the results and the information of the flow near and farter out of the blade surface is very valuable. The blade variation in airfoil, taper, aspect ratio and taper make the use of it very promising and is therefore added to the comparison with engineering codes. Including these more improved aerodynamic codes enhances flow insight and makes derivation of tuning parameters in common engineering codes more consistent, or could give a better idea into possible uncertainties.

The present report only gives a global summary of the most important results as obtained by ECN and DUT. More detailed information can be found in task reports conference papers and journal articles, see e.g. Lindenburg (2003), van Rooij and Schepers (2005), Schepers et. al. (2005) van Rooij (2005), van Rooij and Meng (2006), van Rooij and Meng (2007), Schepers (2007a to 2007c) and van Rooij and Arens (2007).

2. Data used

NREL performed measurements for a wide variety of conditions (tunnel speeds, pitch angles and yaw angles) and different configurations (upwind, downwind, teetered, non-teetered). The data are stored on a (password protected) database. As mentioned in section 1, the focus of ECN's investigations was on the aerodynamic effects at non-yawed flow, yawed flow and fast pitching steps. The focus of DUT's activities was only on the steady state non-yawed inflow with special emphasis on data from the flow over the blade sections which indicated that the flow over the blade is far from steady.

2.1 Data at non-yawed flow as slected by ECN

As a first step in the project, the measurements at non-yawed conditions from the so-called H, I and J sequences have been considered. In these sequences the rotor is rigid (i.e. non-teetered) and located upwind from the tower. The difference between the sequences lies in the pitch angle: The pitch angle for the H sequence is 'nominal', i.e. 3 degrees. The pitch angle for the I sequence is 0 degrees and the pitch angle for the J sequence is 6 degrees.
For every sequence, time series have been selected at tunnel speeds which vary between the lowest possible speed of 5 m/s and the highest possible speed of 25 m/s with an interval of 1 m/s. In all sequences the rotor speed is 72 rpm, which in combination with these tunnel speeds, leads to a relatively low tip speed ratio.

In the analysis of the results, it is important to have a global idea on the local aerodynamic conditions at the different campaigns. Thereto the PHATAS code has been used to calculate the axial induction factor and the angle of attack at 3 radial positions (30% or 47% span, 63% span and 80% span). The results are shown graphically as function of tunnel speed and the three pitch angles in Figure 2-1 and Figure 2-2. As expected the angle of attack increases with tunnel speed and it decreases with pitch angle and radial position. Due to the low tip speed ratio, most angles of attack have already exceeded the (2D) stalling angle of attack of ~ 10 degrees at a tunnel speed of 10 m/s. Furthermore substantial induction factors are only found at a tunnel speed of 5 m/s and a pitch angle of zero degrees. At a tunnel speed of 10 m/s the axial induction factors are between 0.1 and 0.15 and at 15 m/s the induction factors are even < 0.1.

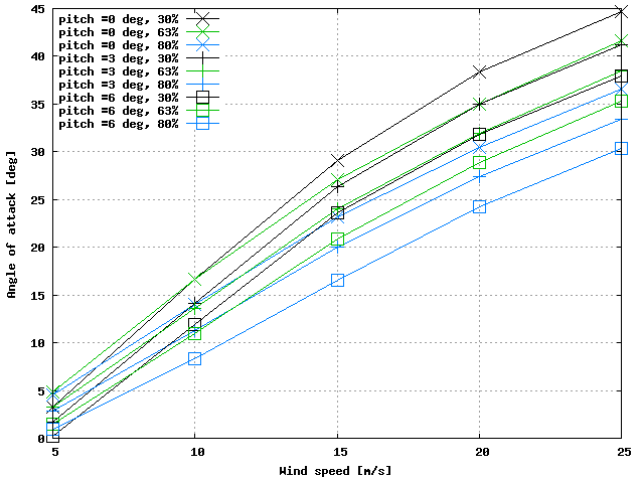

Figure 2-1 Angle of attack calculated by PHATAS for different pitch angles, radial positions and wind speeds

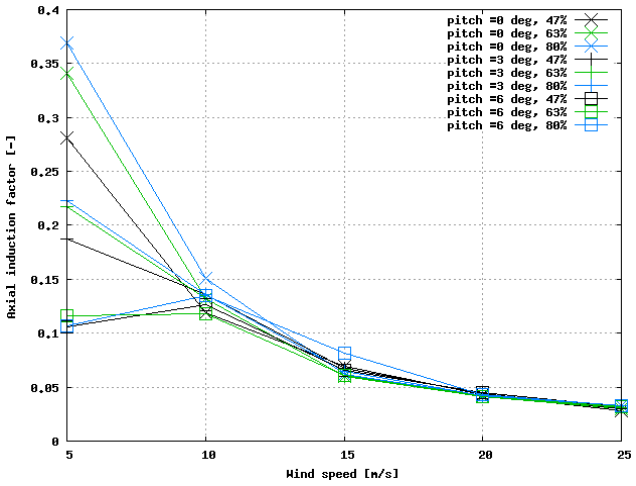

Figure 2-2 Axial induction factors calculated by PHATAS for different pitch angles, radial positions and wind speeds

2.2 The effect of the UAE test set-up on the segment performance

The acquired data from the experiment of the NREL Unsteady Aerodynamics Experiment (UAE) was used in the investigation without additional data reduction. The main focus was on integrated aerodynamic properties like c_n and c_t and the derivatives c_l and c_d.

The 3 non-yawed configurations investigated all having the same blade geometry comprehend:
- The baseline configuration.
- Upwind baseline configuration
- and Upwind configuration with no probes

The measurements were carried out in the NASA Ames wind tunnel for tunnel speeds between 5 and 25 m/s with an increment of 1. m/s. By keeping pitch and rpm fixed several flow conditions over the blade are establish ranging from attached, partly separated to fully separated flow.

Table 2-1 Test configurations

Ordinal number	Test Sequence	Cone Angle	Blade Tip Pitch	RPM
B	Downwind Baseline (Teetered)	3.4 deg.	3.0 deg.	72
H	Upwind baseline (Rigid)	0.0	3.0 deg.	72
S	Upwind, no probes (Rigid)	0.0	3.0 deg.	72

Aerodynamically the main differences between the configurations are downwind/upwind and probes/no probes. The effect of the small cone angle is considered to be negligible.
The teetered connection in B can however initiate unsteady flow behavior in particular when the downwind rotor passes the cylindrical support structure but this effect is probably small and mainly restricted to the lower part of the rotor plane.
Analyzed are the flow parameters, normal and tangential force coefficients, at 5 span-wise locations: 30%, 47%, 63%, 80% and 95%. Determination of the inflow angle was carried out with help of a 5 hole flow probe at 0.8c in front of the leading edge of the blade.

Figure 2-3 shows these coefficients for the test configuration B and H at a tunnel speed of 15m/s. The main difference comes from the location of the rotor which is downwind of the tower for configuration B. At the upwind rotor no periodic upflow disturbances are present as can be concluded from the data of configuration H. The spread in C_n is a little smaller than in configuration B and could be a result of smaller variations in local angle-of-attack established by the rigid blade connection. But still, the variation is large considering that the experiment was carried out at constant tunnel speed and constant rpm.

The average value over all revolutions (approximately 36 revolutions) - which is depicted in bright lines - is for all locations slightly smaller in the upwind configuration H. The difference in level (of e.g. the normal force coefficient) is larger towards outboard. The normal force coefficient is higher then in the 2D wind tunnel tests and indicates augmented lift due to rotation.

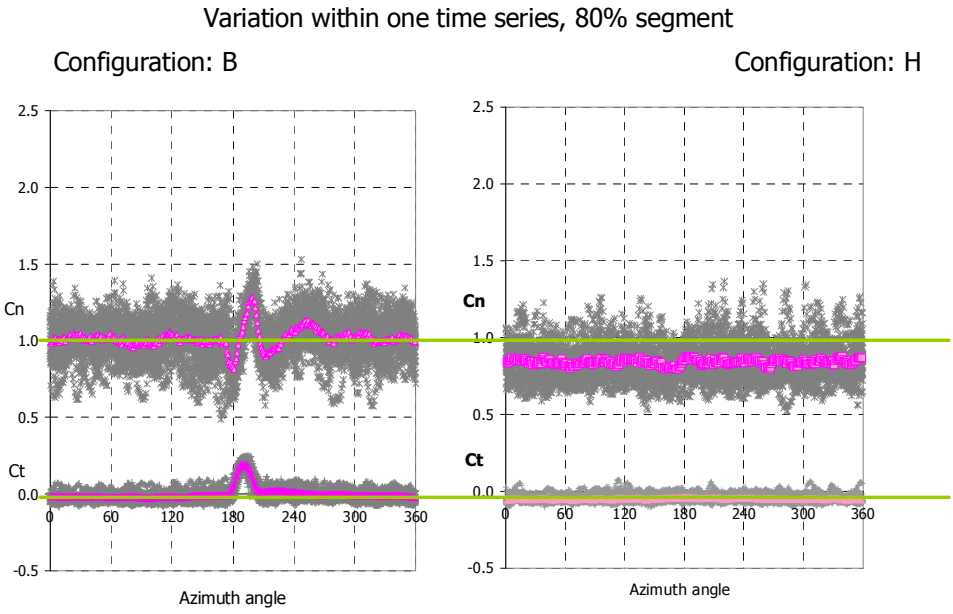

Figure 2-3 The normal- and tangential force coefficient for the test configuration B and H at a tunnel speed of 15m/s

The differences in C_n and C_t are smallest for the upper halves of the rotor plane and this part is (normally) used as reference for the average values.
The average values of the two upwind configurations H and S are compared (against the wind speed) and large variations in C_n for the mid-span and outboard span locations can be observed (Figure 2-4). In general flow probes could result among others in early transition at the blade. This in combination with rotation has been simulated with RFOIL (van Rooij and Timmer (2003), and diminished the influence of the disturbances considerably, similar to what is observed for the inboard positions in this experiment.

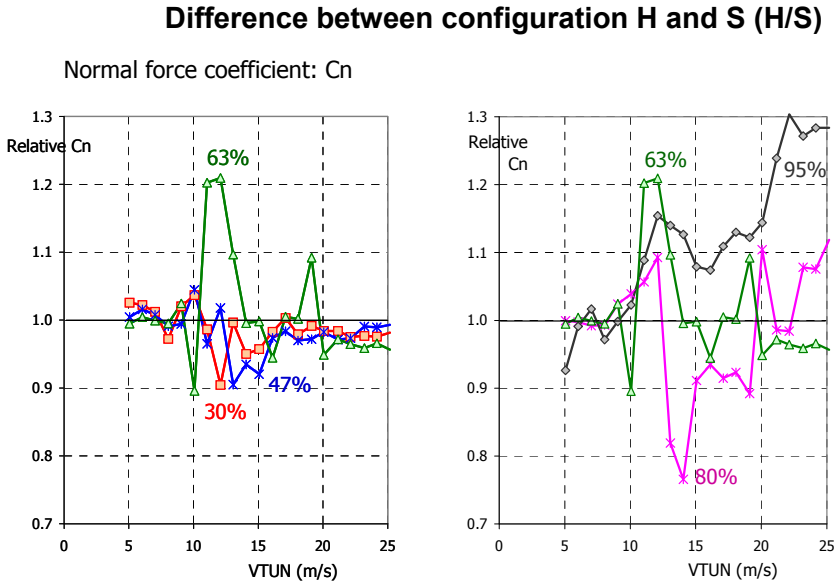

Figure 2-4 The relative normal force coefficients between the H and S configuration for the average data of the upper rotor half

Rotational effects reduces towards the tip and it seems that flow probes have quite some influence in particular at separated flow which is present beyond a tunnel speed of 10 m/s. The most outer segment at 95% shows a continuous increase of the relative normal force coefficient with the S-configuration. There is probably a strong interaction between the disturbances from the probe (at 91% span) and the tip vortex, which increases the C_n values in the H-configuration.

To understand the quality of the dataset and to find the most representative average steady state data some data were research in more detail. Influences coming from the test set-up are then one of the first issues to be investigated. To quantify these effects the rigid blade conditions (H sequence) at a relatively low wind tunnel speed was chosen because the corresponding attached flows respond promptly to small variations in tunnel speed, revolution speed, pitch changes etcetera. This procedure however will not give any information on the accuracy of the measurement system itself.
All segment sections have been investigated and the 30% and 80% span locations represents the overall findings quite well. Within one measurement campaign the rotor speed was (almost) constant at 72 rpm and the effect of tunnel speed variations are then relatively small. The fluctuations in pitch angle were limited to approximately ±0.4 degrees representing a variation of about ±0.04 in normal force coefficient in case of an attached flow.
With the installed pressure system information about the local flow angles (LFA) and pressure distributions were collected. From this the stagnation pressure, the normal force coefficient and tangential force coefficient can be derived and this gives information about variation in flow behavior.

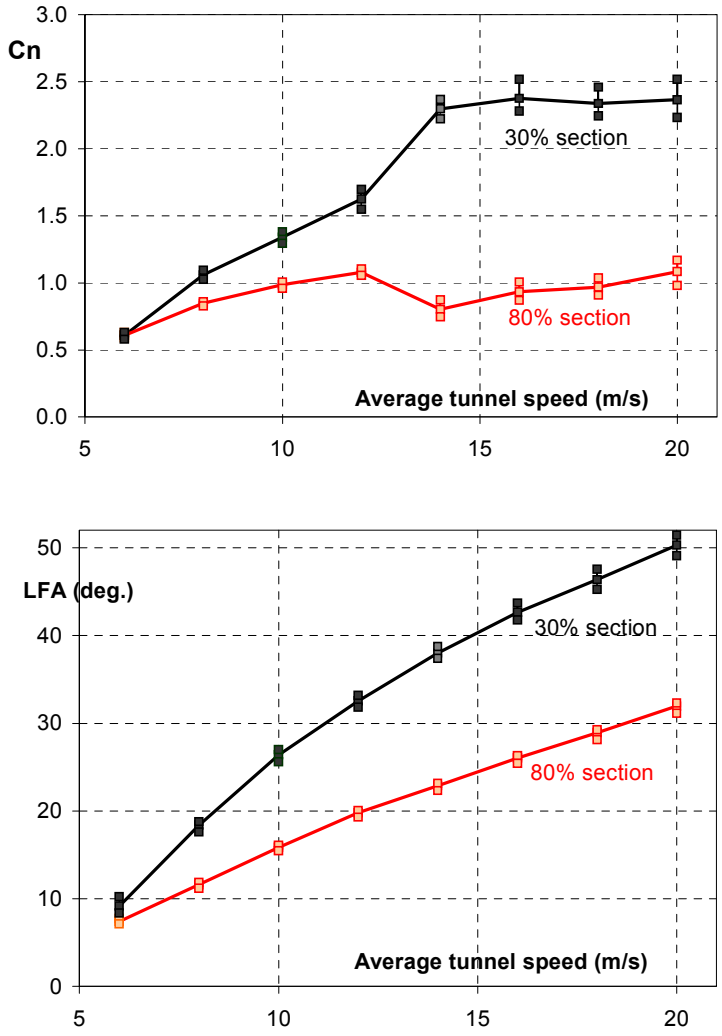

Figure 2-5 Variation of Cn and local flow angle (LFA)

Figure 2-5 demonstrates the variation in C_n with the tunnel speed while the error bars represent the minimum and maximum values of the binned averages. Variation in C_n increases with tunnel speed and beyond a velocity of 12 m/s the error bars become quite considerable. This is in particular true at the inboard segment where the flow is dominated by large turbulent separated areas. This can be deduced from the pressure distributions which indicate leading edge separation at the inboard segment starting at 12m/s tunnel speed. Also the accompanying large LFA values indicate that large inflow angles can be expected.

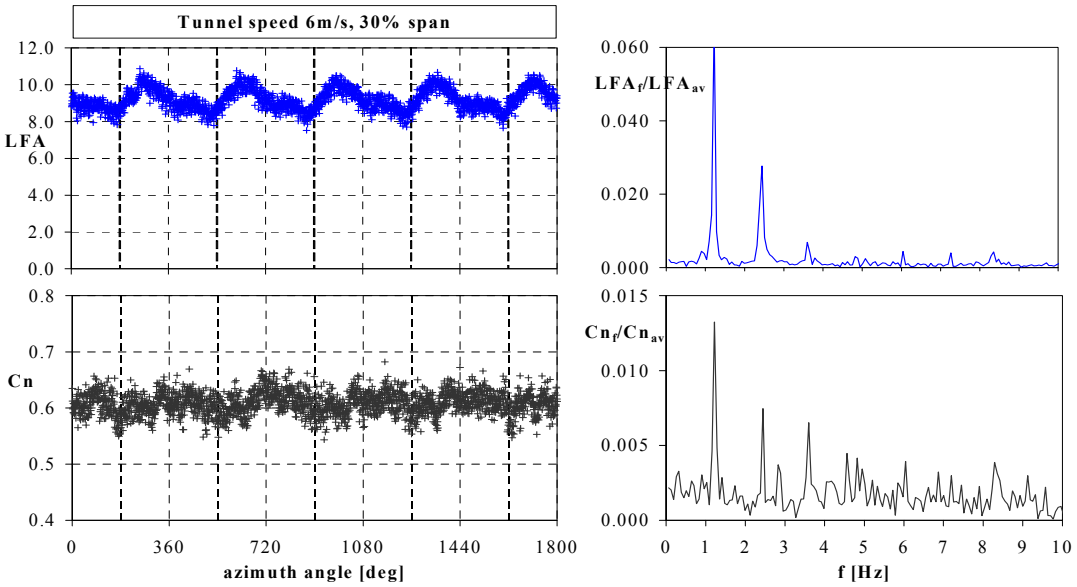

Figure 2-6 The behavior of the local flow angle and normal force coefficient with azimuth angle (a period) and as power spectra for the inboard span position

The variation in normal force coefficient can largely be attributed to the set-up and a representation along the azimuth angle shows this, Figure 2-6. An inquiry with an FFT procedure shows the dominant 1P frequency of peak (1.2 Hz) in the power spectra which corresponds to the blade passing frequency of the instrumented blade. A 2P peak is also very clear at the inboard segment and this represents the blade passing frequency of the rotor, which is 2-bladed. This suggests that the instrumented blade is affected by the non-instrumented blade passing the tower. Structural quantities of the rotor or the control system – which could not fully switched off - could have provoked this. The influences of the tower are smaller, less pronounced, towards the outboard span locations. Higher local velocities and a smaller shadow area probably cause this behavior. At tunnel speeds beyond 12m/s the variations in C_n and LFA and are more random and no clear resonance frequency in the power spectra could be observed. This indicates that flow disturbances caused by flow separation are dominating the flow.

The preceding analysis clearly shows that the set-up affects the acquired data and those representative characteristics for the steady state non-yawed conditions are not easy to obtain extract. Arranging the measurements along the azimuth angle shows some alarming behavior, in particular for LFA between 270 deg. and 360 deg. azimuth angle at the inboard segment (Figure 2-7). This is surprising because only the area coinciding with the tower was expected to be disturbed which is more or less the case at the outboard span position. A comparable behavior was detected for the other segments as-well and was consistent for all tunnel speeds. It seems that a steady behavior of the local flow angle and normal force coefficient, the most important parameters of the characteristics, is achieved in the first quadrant of the rotor plane only.

For proper derivation of the actual Angle-of-Attack a closer look into the flow probes is required. These flow probes were placed slightly outboard the segment orifices and have an inclined angle at the head to increase the range of inflow angles. The measured flow angles (LFA) deviate from those at the segment due to the twist and because it was measured a blade chord in front of the segment. Therefore a correction is needed to associate LFA with the characteristics at the segment.

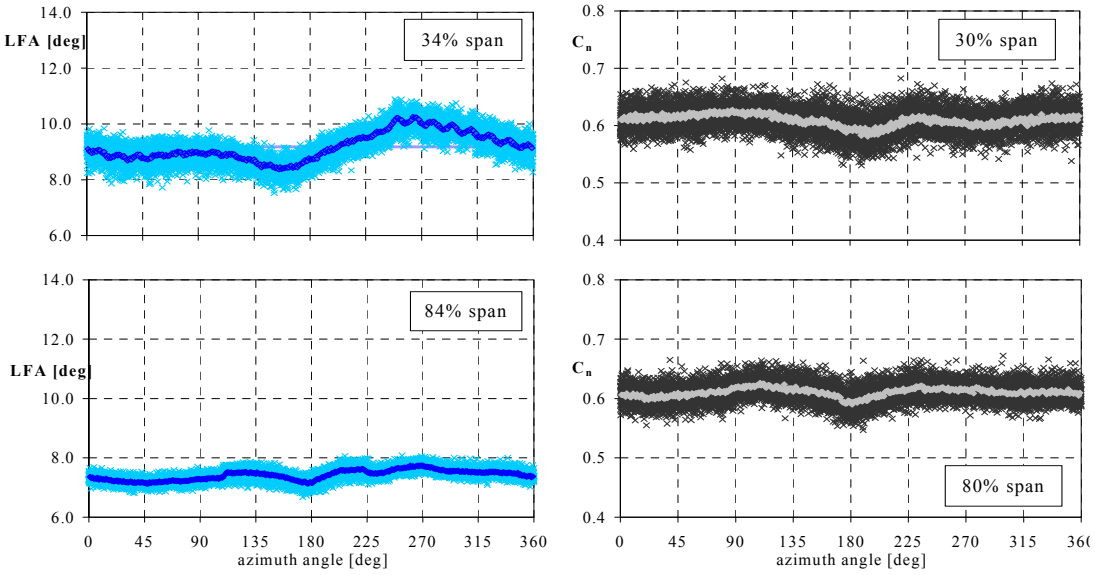

Figure 2-7 The behavior of the local flow angle and normal force coefficient averaged per azimuth angle for the inboard and outboard position

The proposed adjustment of LFA is that of Biot-Savart which corrects for the up-wash caused by the generated lift. This local vortex strength has the largest influence but the flow near the rotor is far more complex. Those contributions are more difficult to estimate and can normally be neglected.

With the correction of the local flow angle, the normal force and tangential force coefficients the segment performance in lift and drag can be calculated. The drag however will not include the skin friction because only pressure distributions were available. The characteristics were derived for the first quadrant of the rotor plane and the results for a tunnel speed of 6m/s are given in Table 2-2. The angle-of-attack (AOA) for this configuration is well below the AOA of 2D stall and attached flow can be expected. Surprising is that C_l varies considerably for an inflow angle of 4deg, C_l= 0.61 against C_l= 0.72. Also the variations in drag are remarkable, especially a 10 times increase between 4.5 and 8.5 degrees is far from common. Drag values are in general small and deviation in inflow angle can lead to substantial changes. Some misalignment of the probes could be responsible for this and an additional correction was proposed and included in the graphs, Figure 2-8.

Table 2-2 Derived segment characteristics along the blade span for two tunnel speeds

	Tunnel speed 6m/s				Tunnel speed 12m/s		
Span location	AOA	Cl	Cd		AOA	Cl	Cd
r/R= 30%	4.5 ^{o}	0.62	0.0037		24.6 ^{o}	1.46	0.673
r/R= 47%	8.5 ^{o}	0.77	0.0419		24.2 ^{o}	1.33	0.582
r/R= 60%	4.0 ^{o}	0.72	-0.0076		16.6 ^{o}	1.19	0.305
r/R= 80%	4.1 ^{o}	0.61	0.0007		14.6 ^{o}	1.09	0.100

The lift and drag at the outboard segment (80% span) are very similar to the 2D measurements. The parts of the lift curves for the attached flow coincide reasonably well with the 2D lift curve except for 47% span location. For increased AOA the more inner sections show a moderate to high increase in lift. This augmented lift due to rotation is consistent with other 3D measurements but the sudden rise for the 30% span location at 25deg. is extraordinary. Strangely the

drag seems not to be affected by this sudden flow phenomenon. The segments with a more moderate increase in lift show a more gradual behavior in lift as-well as drag.

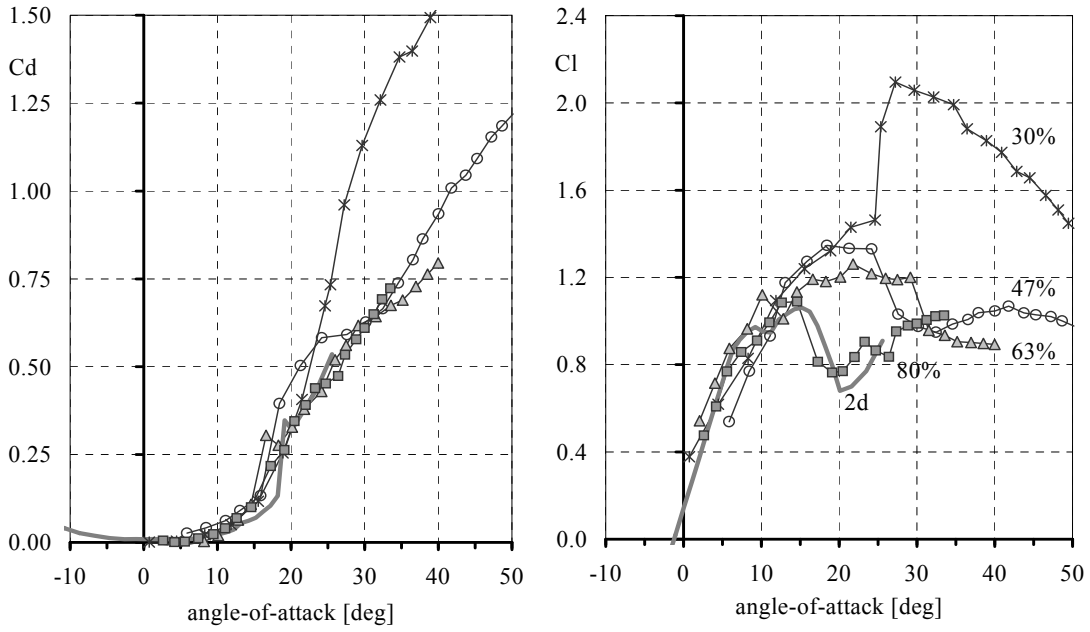

Figure 2-8 The derived drag and lift along the blade with the S809 airfoil

Conclusions and (adopted) recommendations
Analysis of the UAE data series in the configuration with rigid blade, no cone angle, no yaw and upwind rotor on the attached blade flow revealed that:

- the 1P and 2P blade passing frequencies can be observed in almost all aerodynamic parameters for the 4 investigated span locations and is caused by the downwind tower. The variations are most pronounced at the inboard segment.
- the first quadrant of the rotor plane showed the most steady average aerodynamic behavior and should be used by preference to distract the characteristics at the span locations along the blade.

It is recommended to adjust LFA for the 47% and 63% span location. Including investigations of the normal force coefficient in the non-rotating, parked, configuration showed that LFA for these two segments should be corrected with:

- 47% span segment with -3 degrees
- 63% span segment with 1 degrees

Data at non-yawed flow as analyzed by TUD
The non-yawed data played a considerable role in the analyses carried out by Mr. T. Sant as part of his PhD research. Some of it is mentioned in par. 3.2.1 and more can be read in his PhD thesis.

2.3 Data at yawed flow as selected by ECN

In the study on yawed flow, measurements have again been taken from the H, I and J sequences, see par. 2.1. Two yaw angles have been considered: 10 and 30 degrees. In this report, the main emphasis is on the results at 30 degrees. Qualitatively speaking the results for both yaw angles turned out to be very similar (the only difference appears to be in the magnitude of the load variations, which is obviously smaller for a yaw angle of 10 degrees).
It is noted that measurements at very large yaw angles (> 30 degrees) have also been taken, but these are not investigated in the present study.

As mentioned in section 1, the aim of ECN's study on yawed flow, was to investigate the load variations which result from two effects:

- The variation in induced velocity due to the skewed (asymmetric) wake geometry.
- The advancing and retreating blade effect in combination with dynamic stall effects

The first effect mainly plays a role at low tunnel speeds (i.e. high axial induction factors) where the second effect is in particular important at high tunnel speeds.

The minimum tunnel speed at which yawed measurements were carried out was similar to the one for the non-yawed cases (5 m/s), where the maximum tunnel speed was slightly lower (16 or 17 m/s). As explained in par. 2.1, the low rotational speed of the present configuration makes the tip speed ratio relatively low, which in turn leads to a low induction factor and a high angle of attack.

With these considerations in mind, measurements have been selected at V_{tun} = 5 m/s, 10 m/s and 15 m/s for all sequences. The measurements at V_{tun} = 5 m/s are expected to be useful for the investigation of the skewed wake effect on the inflow since the averaged angle of attack is below 5 degrees where the axial induction factor is in the order of 0.2 for case H and 0.3 for case I (see par. 2.1). These axial induction factors are sufficiently high to expect at least some effect from the variation in induced velocity at yawed conditions, where the low angle of attack limits the 'disturbance' from dynamic stall effects.

The measurements at higher tunnel speeds are expected to provide information on the advancing and retreating blade effect in combination with dynamic stall effects, due to the large angles of attack and the low induction.
It is noted that the definitions of yaw angle and azimuth angle as used in this study, differ from the NREL definitions. The actual rotor, placed in the NASA-Ames tunnel rotated anti-clockwise and it applied the zero azimuth angle at the 12 o'clock position. The measurement data have been transformed to a clockwise rotating turbine with zero azimuth at the 6 o'clock position and a yaw angle with sign opposite to the NREL yaw angle.

2.4 Dynamic Inflow measurements as selected by ECN

For the purpose of dynamic inflow analyses, NREL has measured time series at fast stepwise pitch changes.

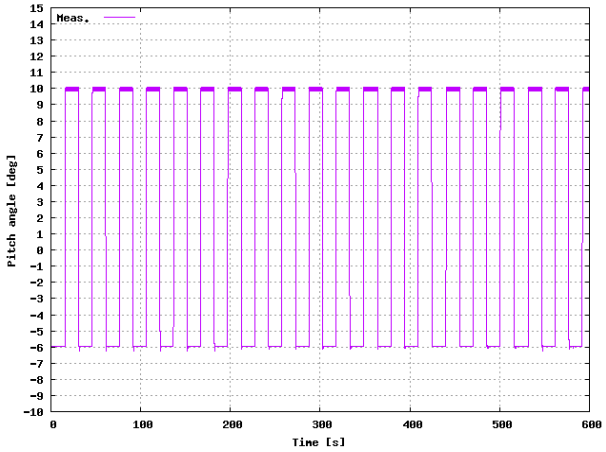

Figure 2-9 Pitch angle variation during dynamic inflow transient

The pitching steps have been performed at different tunnel speeds, but dynamic inflow effects become more prominent at high induction factors. As explained in the previous sections, a high induction factor is associated to a low tunnel speed and for this reason, the time series at the

lowest tunnel speed of 5 m/s (with NREL identification Q0500000) has been requested from NREL.
Figure 2-9 shows the measured time series of the pitch angle at this tunnel speed. The measurement period is 600 seconds and within this period 20 pitch angle steps are performed. Thereto the pitch angle was repeatedly increased with a fast pitching speed from a pitching angle of approximately -5.9 degrees to 10.02 degrees, after which it remains constant for some 15 s. Thereafter it decreases again to a pitch angle of -5.9 degrees.
The axial induction factors (at the instrumented section 30% to 95% span) have been calculated with ECN's aero-elastic code PHATAS. The results are shown in Table 2-3 for the 5 instrumented sections.

Table 2-3 Axial induction factor at fast pitching step

Pitch angle(deg)	a_{30}	a_{47}	a_{63}	a_{80}	a_{95}
-5.9	0.32	0.42	0.58	0.68	1.06
10.02	0.039	0.005	0.008	-0.017	-0.03

It can be noted that the rotor is heavily loaded at a pitch angle of -5.9 degrees but at a pitch angle of 10.02 degrees the rotor is very lightly loaded.
As such the pitch angle steps should be considered as rather artificial but they are very suitable for validation purposes.

In order to smoothen the load signals, ECN applied an averaging procedure, similar to the one used by the Technical University of Denmark in the European Dynamic inflow project (see Snel and Schepers, 1994)). Thereto the different pitching steps are synchronized by initializing them to the start of the pitching step transient. The synchronized, time series are then averaged in order to filter the fluctuations as good as possible. The resulting time series of the pitch angles of both blades, for the upward and downward step are shown in Figure 2-10.

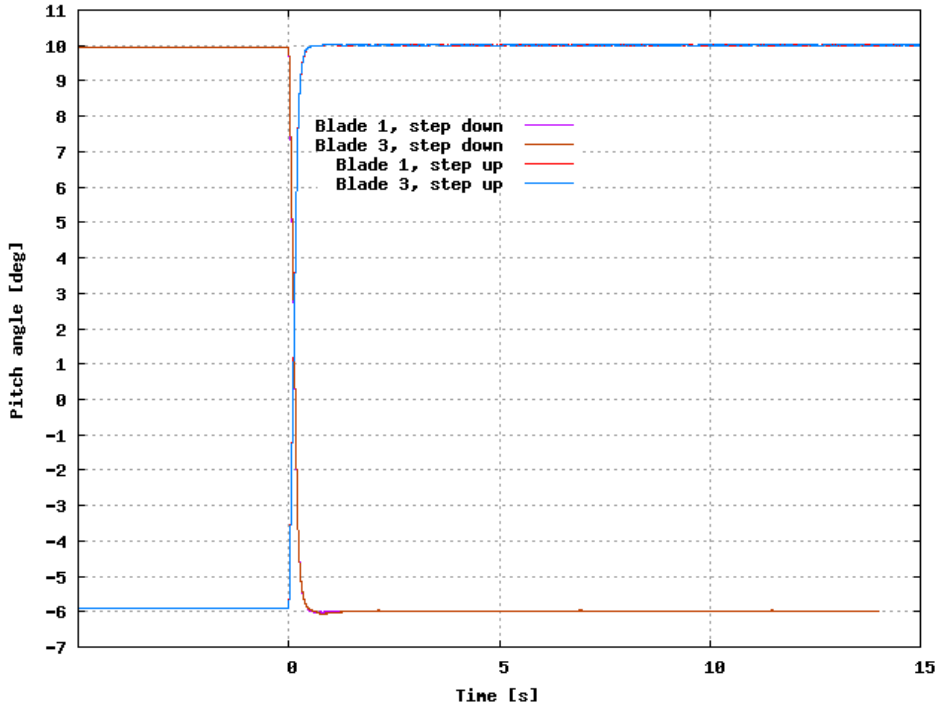

Figure 2-10 Pitch angles of both blades, averaged over all transients, for upward and downward pitching step

3. Methods employed

3.1 Methods employed by ECN

The main activities which were performed by ECN consisted of a comparison of the NASA Ames measurements with calculated results from two of ECN's codes:

- The aero-elastic wind turbine design code PHATAS. This code has been used to calculate all the measurement cases.
- The free wake lifting line code AWSM. This code has only been used to calculate the cases at low tunnel speeds. At yawed conditions and high tunnel speeds AWSM did not reach a convergent solution. Although a convergent solution was reached at the aligned cases and high tunnel speeds, the results are not presented because the angle of attack exceeds the stall angle of attack where, in principle, AWSM does not account for stall effects. Furthermore it must be noted that the potential advantage of AWSM lies in its calculation of induction. As such, a comparison between AWSM and the measurements makes most sense for conditions where the induction is relatively large, i.e. for low tunnel speeds (Figure 2-2).

3.1.1 PHATAS

The calculations in the present report have been performed with a PHATAS release "Apr-2005". This version of the code is documented in Lindenburg (2005).

The following remarks can be made on the PHATAS simulations:

- The input on the NREL wind turbine is based on the description given in Lindenburg (2003). Several degrees of freedom are taken into account, e.g. the blade flexibility in the edgewise and flatwise direction, blade torsion, shaft torsion and the dynamics of the tower. Furthermore the asynchronous generator has been modeled;
- The tunnel speed is assumed to be homogeneous and constant in time. Tower shadow has been included;
- The pitch angle is assumed to be constant (except for the dynamic inflow transients, where the measured time series of the pitch angle is prescribed)
- The calculations have been performed over a period of 20 s (except for the dynamic in-flow transient where the measured time series is simulated)
- The aerodynamic modeling of PHATAS is based on the blade element momentum theory. This requires tables of aerodynamic characteristics (i.e. $c_l(\alpha)$,$c_d(\alpha)$ and $c_m(\alpha)$). It is noted that the aerodynamic airfoil along the blade is the NREL S809 profile.
- The 2D, stationary (non-rotating) aerodynamic characteristics of this airfoil have been constructed by combining wind tunnel measurements from the University of Delft with wind tunnel data from Ohio State University. The data have been extended to deep stall according to the methodology as described in chapter 2 of Lindenburg (2003). The resulting 2D aerodynamic characteristics are presented in the Figure 3-1and Figure 3-2.
  3D effects in stall are accounted for by the model from Snel et. al.(1993). In this method a factor f_{cl} is used to correct the 2D lift coefficients $c_{l,2D}$. The factor f_{cl} is the ratio of the actual increase in cl (i.e. $c_{l,3D}$ - $c_{l,2D}$) and the difference dc_l between the non-viscous lift coefficient, $c_{l,potential}$ (with 'potential' slope $dcl/d\alpha = 2\pi\alpha$ and the 2D value of $c_{l,2D}$. Hence:

  $$c_{l,3D} = c_{l,2D} + f_{cl} (c_{l,potential} - c_{l,2D})$$

  The factor f_{cl} is given by:

  $$f_{cl} = 3 (c/r)^2$$

  Note that the method only corrects the lift coefficients and not the drag nor the moment coefficients.

- Dynamic stall is modeled with the first order dynamic stall model from Snel (1997). Again it is only the lift which is corrected.

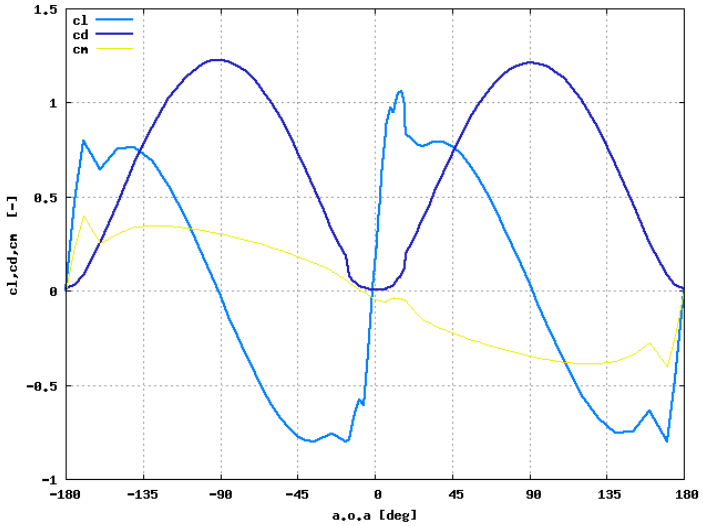

Figure 3-1 S809 airfoil: Basic 2D aerodynamic coefficients for -180 < θ < 180

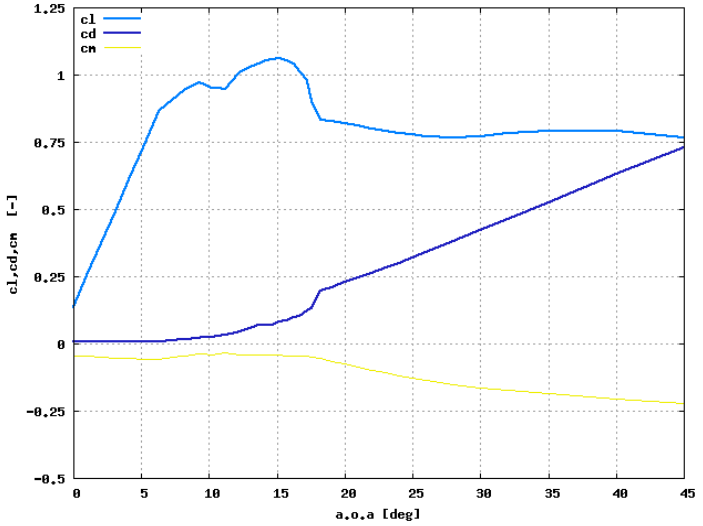

Figure 3-2 S809 airfoil: Basic 2D aerodynamic coefficients for 0 < θ < 45

3.1.2 AWMS

The AWSM code, see van Garrel (2003), is based on a non-linear lifting line vortex wake theory. The code is of a free wake character but for distances larger than 4 rotor diameters downstream of the rotor, the wake is assumed to be 'frozen'.

The blades are modeled as lifting lines. This implies that, similar to the PHATAS code, aerodynamic profile data should be prescribed as function of the angle of attack. Thereto the same airfoil data as used in PHATAS have been applied. 3D and dynamic stall corrections are not taken into account (although instationary effects which result from the shed vorticity are modeled).
In principal a 3D stall correction could be added to the airfoil characteristics, but AWSM has only been used to simulate low tunnel speed cases, for which stall corrections are less relevant.

The AWSM calculations were made under the following assumptions:
- The construction is assumed to be rigid and mass induced loads are neglected
- The wind speed is constant in time and homogenous; the aerodynamic tower shadow effect has been neglected.
- The rotor speed and pitch angle are constant (except for the dynamic inflow transient where the measured pitch angle is prescribed).
- The calculations have been performed over a period of 11 seconds (except for the dynamic inflow transient where the measured time series is simulated).

Many improvements have been made to ASWM, mainly on the field of the numerics, in order to make it robust for the present calculations. However the calculations at yawed flow and high wind speeds still did not reach a convergent solution.

3.1.3 Procedure of the comparison between calculated and measured results

The comparison between calculations and measurement at non-yawed conditions are mostly made in terms of mean blade segment loads (normal and tangential forces), flatwise moments at the blade root and the rotorshaft torque, i.e. the values are averaged over the calculations or measurement time. It is emphasized that such comparison is based on dimensional quantities which are calculated at given external conditions (although the comparison on normal and tangential forces is made in terms of $c_n(c_t).0.5\rho V^2$ which differ from the actual forces through the (constant) value of the chord).
Such comparison avoids the uncertainty in the measured angle of attack and dynamic pressure which is experienced in case the comparison is made in terms of dimensionless aerodynamic characteristics as function of the angle of attack, see e.g. Schepers et. al.(2002).
The comparison at yawed conditions is mostly made in terms of azimuthally binned averaged values. The comparison of the dynamic inflow cases is made on basis of time series, where the averaged measured pitch angle step has been prescribed to PHATAS and or AWSM.

3.2 Methods employed by DUT

3.2.1 Derivation of the Angle of Attack using a Free-Wake Vortex Model

Experimental Data used
This study used the experimental data collected from the NREL Phase VI rotor when operating in the 'S' configuration in the NASA Ames wind tunnel.
The analysis was performed at various wind speeds yielding attached and stalled flow conditions over the blades. Both axial and yawed rotor conditions were studied, as follows:
(i) Yaw 0^0 – U = 5, 7, 10, 13, 15, 20 and 25m/s
(ii) Yaw 30^0 – U = 5, 7, 10, 13 and 15m/s

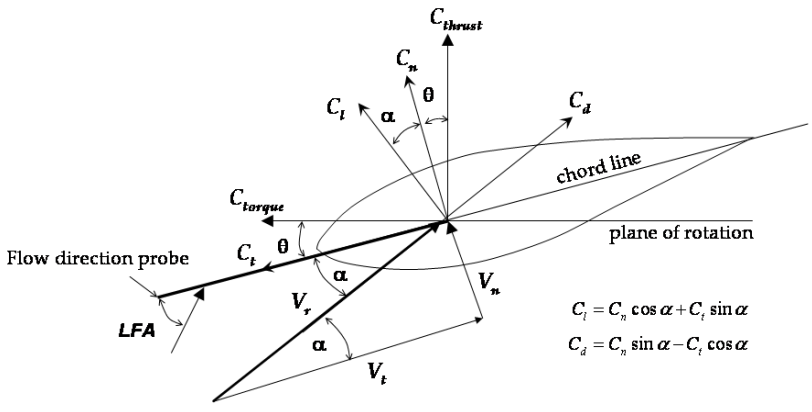

Figure 3-3 Blade section aerodynamic load coefficients

Method
A novel and comprehensive methodology was adopted by using the blade pressure measurements in conjunction with a free wake vortex model to estimate the angle of attack (definition given in Figure 3-3) at the blades more accurately, together with the induced velocity distributions at the rotor plane and the wake geometry.

This methodology consisted of the following sequence of steps: Initially, a span-wise distribution for the angle of attack was assumed blades as-well as C_n and C_t which were used to determine the lift coefficients at the blades. Using the Kutta-Joukowski law, the bound circulation distribution at the blades was determined and prescribed to the free wake vortex model to generate the free vortical wake. The induced velocity at the blades was estimated and used to calculate a new angle of attack distribution. The process was repeated until convergence in the angle of attack was achieved. One advantage for applying this methodology is that the solution is in itself unsteady and could be readily applied to yawed conditions, under which complex aerodynamic phenomena are known to occur (e.g. dynamic stall and unsteady induction). A second advantage concerns the fact that the wake geometry is inherently part of the solution. Thus it is possible to derive the pitch and expansion of the helical wake from the measured C_n and C_t.

The free wake code applied was created at Delft University of Technology. The code was specifically designed to model rotor wakes in both axial and yawed conditions from knowledge of the aerodynamic loads on the blades. The input to the code is a prescribed span-wise distribution of bound circulation instead of normally the airfoil characteristics. From this prescription, the code will generate the lifting line values and the vortex wake sheets and calculates the 3D induced velocities at the rotor plane. The near wake consists of vortex sheets, one per blade, modeled as a mesh of straight line vortex filaments to account for trailing and shed vorticty. The far wake model consists of a helical tip vortex at each blade, representing the fully rolled up tip vortices. Each helical tip vortex is attached to the outboard end of the corresponding near wake. It is assumed that, at the transfer of the near to the far wake model, each near wake vortex sheet rolls up immediately into a concentrated tip vortex. This assumption is not physical but was found to yield accurate predictions for the inflow at the rotor plane and near wake geometry in a validation study performed on the subject free wake vortex model.

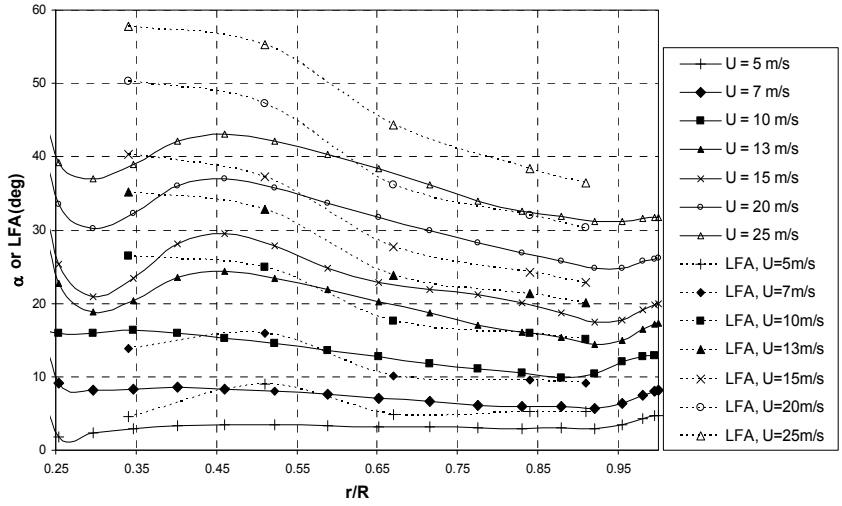

Figure 3-4 Converged angle of attack distributions at different wind speeds for Yaw 0^0. The LFA values measured with the probes are also shown

Axial Conditions (Yaw 0^o)
The converged angle of attack distributions for axial conditions are shown in Figure 3-4. The experimental values for the local inflow angles at the probe tips are also shown at each wind

speed. Large differences are observed between the computed angle of attack and the measured LFA results.

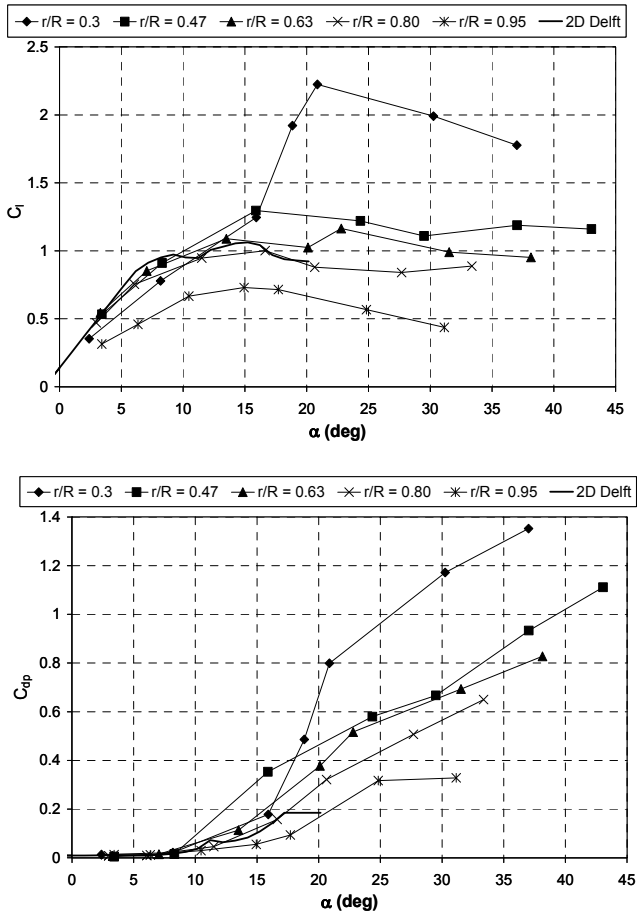

Figure 3-5 Derived lift and drag coefficients for different radial positions for Yaw 0^0

Figure 3-5 summaries the aerofoil data derived from the measured values of C_n and C_t and the angle of attack distributions of Figure 3-4. Both the lift and drag coefficients are dependent on the radial location. The 2D Delft wind tunnel data for the S809 aerofoil are plotted for a Reynolds number of 1.e6. The derived lift and drag coefficients were used together with the calculated induced velocities at the blades to calculate the low-speed shaft torque (LSSTQ) and the blade root-edge moments (RFM and REM). These were compared with those measured experimentally using strain gauges (Figure 3-6). The latter are plotted together with the corresponding ±1 standard deviations. The large standard deviations in the REM were due to the cyclic gravitational loads. The aerodynamic loads were also derived directly from the pressure measurements by calculating the torque and thrust coefficients at each blade element and integrating across the whole blade. These compared very well with those calculated by the free wake code but not so well with those measured with strain gauges. Most probably this is mainly due to errors in the measured values of Ct.
Finally, the derived C_l-α and C_d-α data were used in a BEM model to compute the same global loads. It was found that whether to include the Prandtl tip/root loss factor or not did not have a significant difference on the global load predictions.

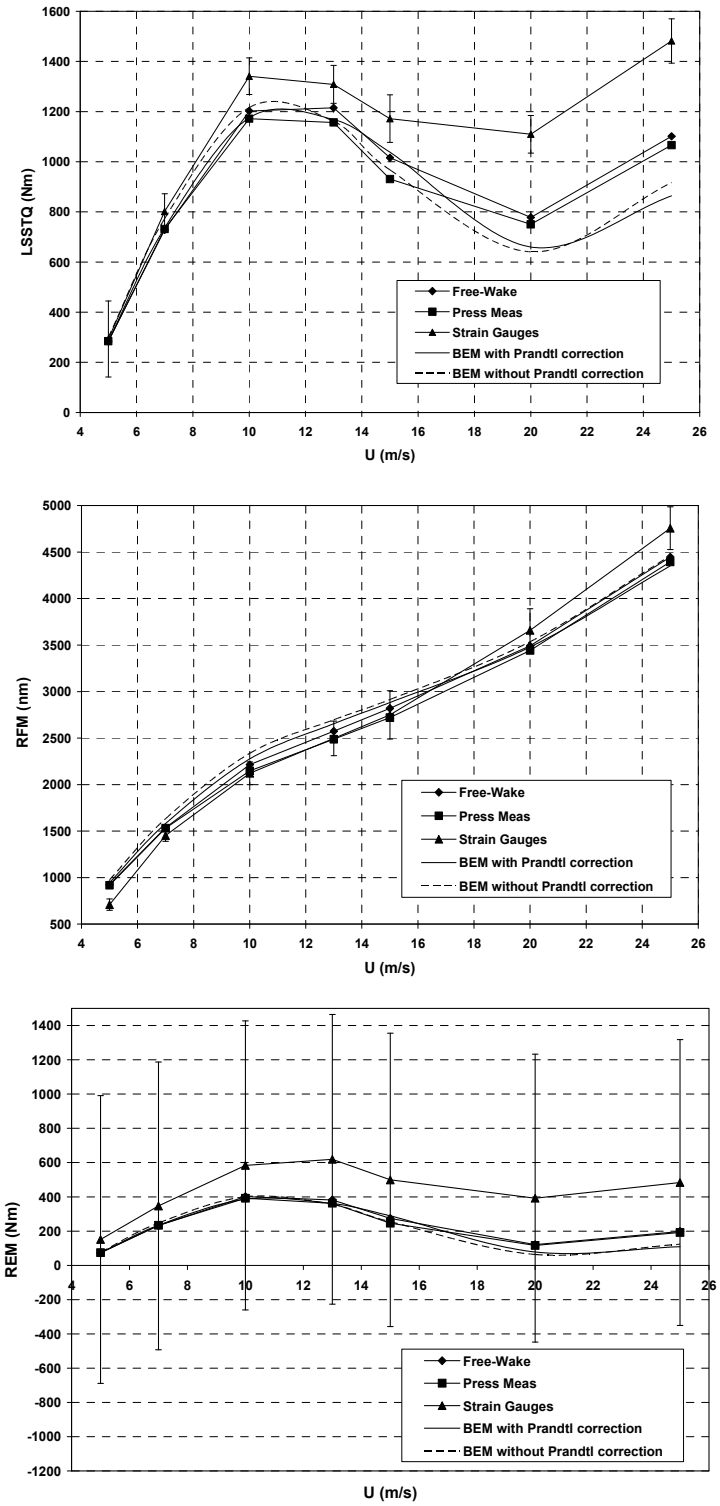

Figure 3-6 Torque (up), flapping moment (middle) and edge moment(bottom) in relation to tunnel speed

Yawed Conditions (Yaw 30^o)

Figure 3-7 illustrates the converged angle of attack variations with the blade azimuth angle at U= 10m/s. The measured LFA values are also shown.

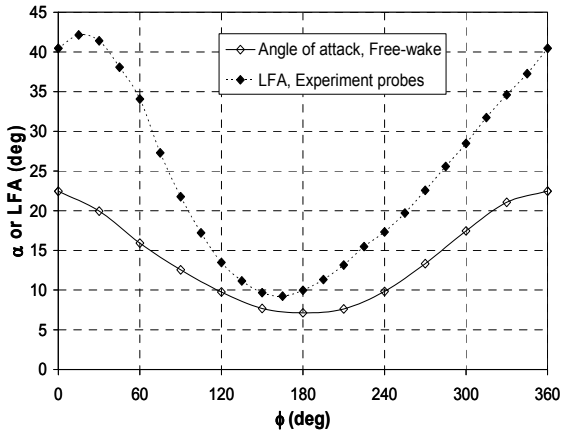

Fig. (a): r/R= 0.34

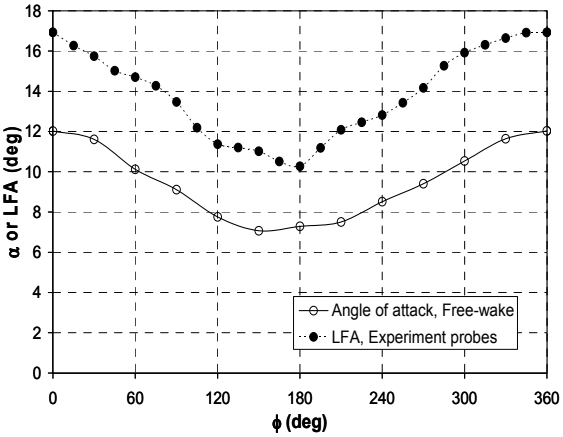

Fig. (b): r/R= 0.84

Figure 3-7 The LFA and derived angle-of-attack for U= 10m/s at yaw= 30^o.

Large differences are noted between the angle of attack and the corresponding LFA values at all azimuth positions of the blades, similar to what was noted in axial conditions. Yet one should also keep in mind that in yawed conditions, the probe was subjected to highly unsteady flow situations.

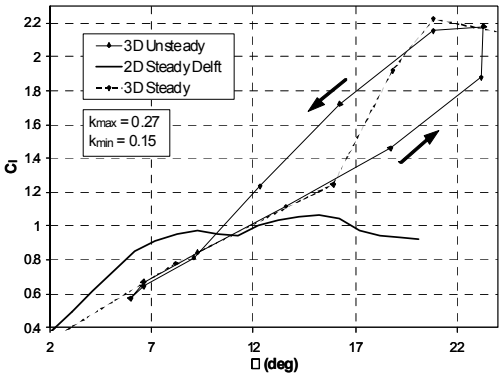

Fig. (a): r/R= 0.3

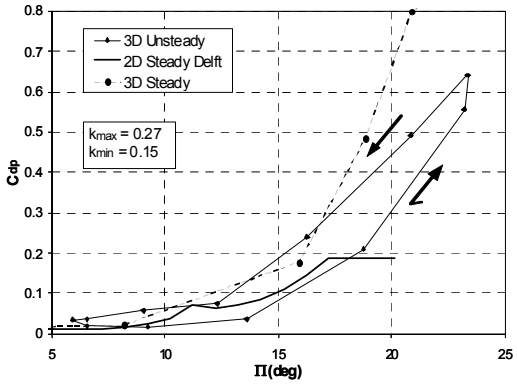

Fig. (b): r/R= 0.3

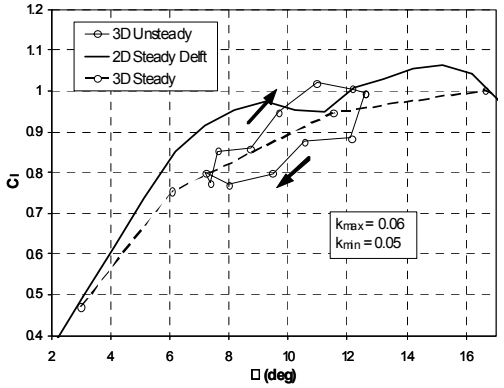

Fig. (c): r/R= 0.8

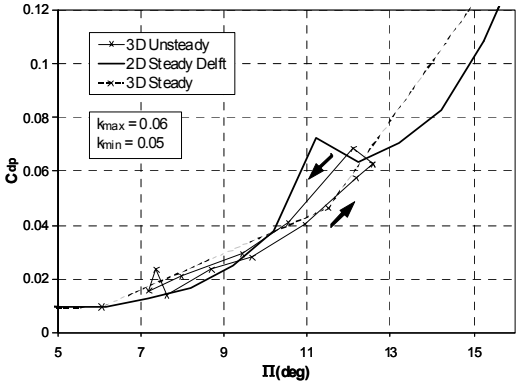

Fig. (d): r/R= 0.8

Figure 3-8 C_l-α and C_d-α hysteresis loops for U= 10m/s and yaw angle of 30^o.

At U=10m/s, the free wake model estimated that the time rate of change of angle of attack reaches a peak of about ±78 deg/s at the inboard sections. Further work is required to establish the accuracy with which five-hole pressure probes manage to measure the LFA at such high levels of unsteadiness.
From the variations of C_n and C_t obtained from the blade pressure measurements and the results for the angle of attack presented in Fig. 3-5, it was possible to derive the unsteady aerofoil hysteresis loops for C_l-α and C_{dp}-α. Figure 3-8 illustrates the hysteresis loops for different radial locations at U=10m/s, Yaw 30^o. The 2D steady aerofoil data obtained from the Delft wind tunnel experiments are also shown. The 3D steady aerofoil data, which were derived using the blade pressure measurements for non-yawed conditions together with the free wake code are also included. One should keep in mind that in a yawed rotor, these loops are not only due to cyclic angle of attack variations, but also due to a cyclic variation of the flow velocity relative to the blades. In each of these hysteresis plots, the reduced frequency k is included ($k = \Omega c/(2V_r)$). It was observed that the hysterisis loops often change direction from counter-clockwise to clockwise when moving outboard from r/R=0.3 to 0.95 (see Figure 3-8).

Conclusions

1. Using a free-wake vortex model it is possible to derive the angle of attack at the blades from blade pressure measurements in both axial and yawed conditions. With help of the derived angle of attack and the measured C_n and C_t values, new 3D steady and unsteady aerofoil data can be obtained.
For axial conditions in which the angle of attack is steady, the following conclusions could be made:
- for small angles of attack (less than the 2D static stalling angle), the new 3D aerofoil data is very close to the 2D aerofoil data except at the tip and root region. In the latter regions, the new 3D lift coefficient was found to be lower than the 2D aerofoil data.
- for larger angles of attack, the new 3D aerofoil data was considerably different than the 2D data and the presence of stall-delay was evident, especially at the inboard sections of the blades.

It was also observed that the increase in the lift coefficient due to stall delay is accompanied by a corresponding increase in the drag coefficient.
For yawed conditions in which the local angle of attack is unsteady and a function of the blade azimuth angle, the following conclusions could be drawn:
- the 3D unsteady coefficients could well exceed the corresponding steady values derived for axial conditions.
- the unsteady C_l-α and C_{dp}-α hysterises loops were in general closer to the 3D steady values than to the corresponding 2D steady data. This was observed at both attached and stall conditions and it implies that 3D effects (in particular stall-delay) have a significant role in the unsteady flow behavior of wind turbine blades.

2. With a free-wake vortex model it is also possible to derive from the blade pressure measurements the complex 3D induction at the rotor plane together with the wake geometry and circulation distribution. These are vital in order to have a better understanding of a wind turbine's aerodynamic behavior in both steady and unsteady environments.
3. Given that reliable 3D aerofoil data is available, BEM predictions for wind turbines improve significantly, even for conditions of deep stall and rotor yaw. In many situations, BEM results for the blade aerodynamic loading distributions are unreliable not necessarily because the BEM theory is deficient but because incorrect aerofoil data is used.
4. When using 3D lift and drag aerofoil data derived directly from the blade pressure measurements, the tip/root loss correction model is no longer required in the BEM calculations. This is because the tip/root loss effects are already accounted for in the 3D aerofoil data.

3.2.2 The Effect of Blade Geometry on the Normal Force Distribution of a Rotating Blade

The effect of rotation on the segment C_n characteristics has been investigated with emphasis on the blade layout. A standard engineering model was used as reference with the aim to derive the tuning parameters related to the 80% blade segment performance. Three blade layouts were available being a blade with constant chord without and with twist, and a tapered blade with twist and were designated as phase II, III, IV and phase VI respectively (see Table 3-1 for the blade data). So, only the latter was part of the UAE experiment which was reference in this IEA Annex.

Table 3-1 Main blade parameters

Phase	**II**	**III-IV**	**VI**
c/R= 0.30			
c/r	0.305	0.305	0.438
Twist angle	0.0	24.2	7.4
Pitch angle*	12.0	3.0	3.0
c/R= 0.47			
c/r	0.195	0.195	0.243
Twist angle	0.0	12.7	2.0
Pitch angle*	12.0	3.0	3.0
c/R= 0.63			
c/r	0.145	0.145	0.156
Twist angle	0.0	6.8	0.24
Pitch angle*	12.0	3.0	3.0
c/R= 0.80			
c/r	0.112	0.112	0.101
Twist angle	0.0	2.8	-1.1
Pitch angle*	12.0	3.0	3.0
c/R= 0.90	N/A	N/A	N/A
* Average value during the campaigns			

The focus in this investigation is on the steady state non yawed inflow conditions. Determination of such at the test field took quite some time not only due to wind variations but also because in the field tests the rotors were downwind. At the field measurements most of the time series could not be used fully but still the amount derived was sufficient for a proper investigation. In all cases the first quadrant of the rotor plane was used and averaged.
Also measurements of the inflow angles were different. In Phase II and III a flag measurement device was used to determine the inflow angle while the later campaigns were carried out with a (5-hole) flow probe.

Reference engineering Model

Most of the steady state stall models for adjusting the 2d airfoil characteristics due to rotation have the basic form of Eq. (1).

$$c_{l,3D} = f \;.\; (c_{l,inv} - c_{l,2d}) + c_{l,2d} \qquad (1)$$

In Eq. (1) the inviscid lift ($c_{l,inv}$) is sometimes exchanged with the extension of the linear part of the viscous lift gradient. The parameter f is related to the local solidity c/r and sometimes a twist (plus pitch) term is added. Hence f can be represented by $f = F_1(c/r).F_2(\text{twist} + \text{pitch})$.
Rewriting the equation such that the lift coefficient can be exchanged with the normal force coefficient enables direct application of the measured values in the equations which is of great advantage. For the lift coefficient one can write:

$$c_l = c_n \cos(\alpha) - c_t \sin(\alpha) = \frac{c_n}{\cos(\alpha)} - c_d \tan(\alpha) \qquad (2)$$

The latter part of Eq. (2) can be substituted in Eq. (1) and subsequently converted to a relation in f on the left-hand side. Then the numerator contains the term $(c_{d,3D} - c_{d,2d})*\sin(\alpha)$ which is zero in most of the stall models. This term was found to be small compared to the normal force coefficients and neglecting is acceptable. Additional exchange of c_d in the denominator with c_n and c_t will give Eq. (3) as function of f.

$$f = \frac{c_{n,3D} - c_{n,2d}}{c_{l,inv}\cos(\alpha) - c_{n,2d}(1 - \sin^2(\alpha)) + c_{t,2d}\sin(\alpha)\cos(\alpha)} \qquad (3)$$

The latter part in the denominator with ct is always small even up to high angles-of-attack because in particular at leading-edge stall c_t is close to zero. The term $\sin^2(\alpha)$ increases with higher inflow angles and its contribution can not be neglected beyond approximately 20 deg. For the S809 airfoil this second term in the denominator is approximately 5 times larger then the last term with c_t. The same holds for 25 degrees and it is recommended to neglect only the last term in the denominator. Now the 3D normal force coefficient becomes Eq. (4).

$$c_{n,3D} = f * (c_{l,inv}\cos(\alpha) - c_{n,2d}(1 - \sin^2(\alpha)) + c_{n,2d} \qquad (4)$$

Application of the Model

Equation (4) only contains measured characteristics and this will be used to compared all blade layouts. The 2D normal force coefficients are usually taken from the wind tunnel experiment, but in this case they are exchanged with the 80% segment c_n. Figure 3-9 shows the difference between the measured 2D c_n. The right graph shows the values for the denominator in equation 3 compared with the results of the 80% segment. Extension of the 2D relations for higher angles-of-attack is very convenient.

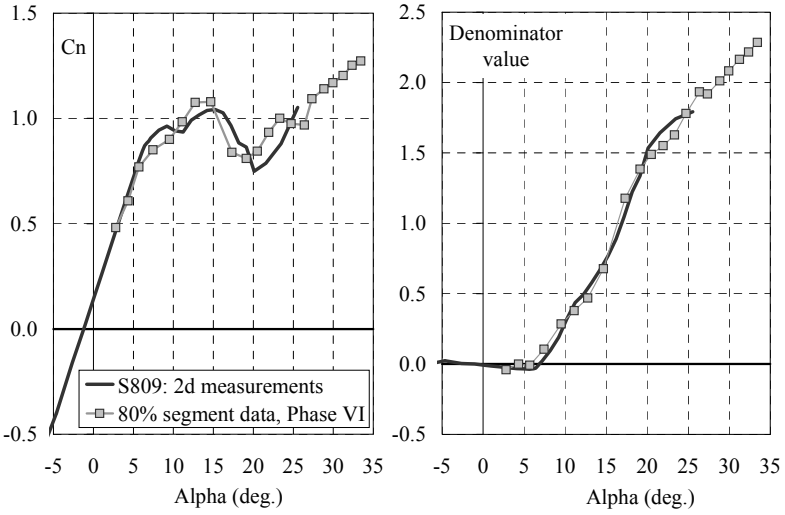

Figure 3-9 Similarity between the wind tunnel and 80% segment performance.

Now Eq. (3), which describes the behavior of the normal force coefficients in rotational flow, can be exchanged with Eq. (5):

$$f = \frac{c_{n,3D} - c_{n,80\%}}{(c_{l,inv}\cos(\alpha) - c_{n,80\%}(1-\sin^2(\alpha))} \qquad (5)$$

The exchange of $c_{n,2d}$ with cn,80% is fair for all the configurations and will be confirmed later. This leads to the denominator depicted in Figure 3-9. The reference angle-of-attack is also from this 80% segment.
In principle, all terms can now be expressed in c_n values and inflow angles of one measurement campaign.

The Segment Normal Force Coefficients
The angle-of-attack can not be measured directly and is derived from the with the probe measured local flow angle (LFA). The main influence is from twist and up-wash which has been determined with the normal force coefficient (instead of the lift).
The distribution of the normal force coefficients are represented by trend lines for each segment and phase, and reflects an average behavior. Figure 3-10 shows these lines for c_n with corrected inflow angle compared with the 2d measurements for the inboard and mid-span segments for the 4 different measurement series. Surprisingly there is a difference in characteristics between configuration III and IV and this can only be attributed to interference effects of the different measurement devices in particular for monitoring the inflow angle. These blades have exactly the same geometry and therefore in the overall comparison the average of these two phases will be used and is designated as III-IV or in short III.

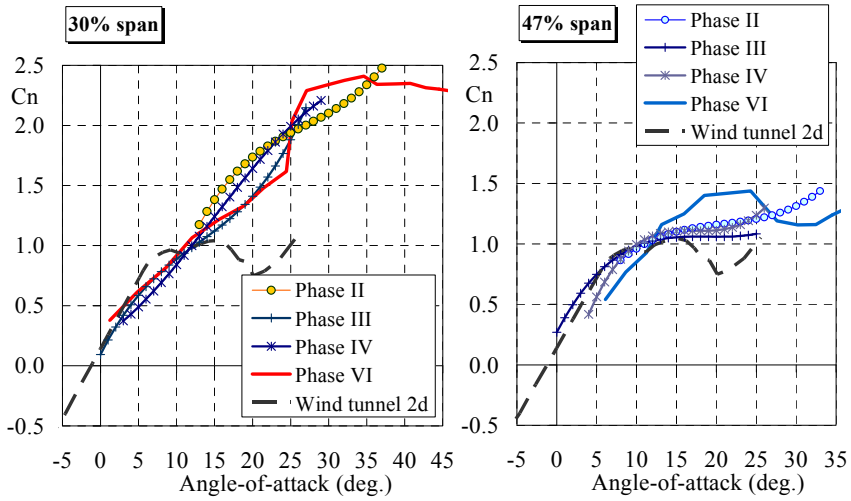

Figure 3-10 The trend line cn for inboard and mid-span.

The dependency of the Normal Force Coefficient with the Blade Geometry
The derived trend lines are used as input to find out the difference in normal force coefficient for the different blade geometries for the 5 span positions (3 are given in Fig. 3-9). Important is further that the 80% span data is assumed to be the same in all blade configurations and this becomes the connection the behavior of the local blade information (caused by rotation of better augmented lift). The comparison can then be carried out along the general formulation of the stall models according to Eq. (5). The denominator is exchanged with the data for the 80% segment and phase VI is the reference. Now, values are available over a large range of angles-of-attack.
For the inboard (30%) segment of phase II Eq. (5) becomes;

$$_{II}f = \frac{_{II}c_{n,30\%} - _{II}c_{n,80\%}}{(c_{l,inv}\cos(\alpha) - _{VI}c_{n,80\%}(1-\sin^2(\alpha))} \qquad (6)$$

Comparison of the difference in f from the measurements between two configurations can then expressed by:

$$_{II}f - _{III}f = \frac{_{II}c_{n,30\%} - _{III}c_{n,30\%}}{\text{Denominator}} \qquad (7)$$

Comparison with Engineering Stall Models

The backbone in the comparison is parameter f which represents the augmented lift due to rotation and is defined in equation1 and is related to the local solidity c/r and sometimes a twist (plus pitch) term is included. Hence f can be represented by $f = F_1(c/r).F_2(twist + pitch)$.
Because the blades of phase II and III-IV have the same chord (so F_1 is the same) the difference between these phases can be analyzed with:

$$_{II}f - _{III}f = _{III}F_1.(_{II}F_2 - _{III}F_2) \qquad (8)$$

This should result in a constant per span location because F_1 and F_2 are assumed to depend on the blade geometry only. Figure 3-11 clearly shows that such can not be the case and a dependency in either F_1 or/and F_2 with the inflow angle need to be present.

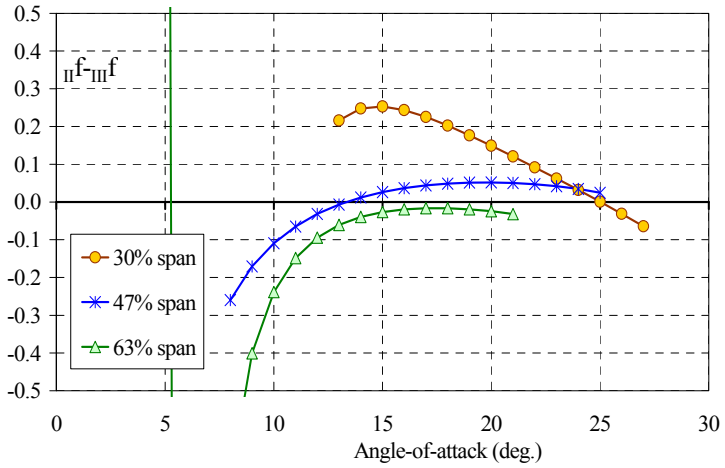

Figure 3-11 The difference in 3D correction factor f for phase II and III-IV as function of the inflow angle

The comparison for *f* between phase VI and phase III-IV can be evaluated in the same way with:

$$_{VI}f - _{III}f = _{VI}F_1.{}_{VI}F_2 - _{III}F_1.{}_{III}F_2 \qquad (9)$$

If twist+pitch were the same in both configurations the equation could be reduced further. Again, the outcome is constant since no dependency with inflow angle is included. Confirmation of twist+pitch shift with inflow angle was already been indicated by Schepers et. al. (2004) through analysis of cn-α curves on the phase VI blade geometry. Such relation will however severely complicate tuning of the correction parameters.

The engineering stall models used here are described by [10]:

$$f = A.(c/r)^B * \cos^n(\varepsilon + \theta) \qquad (10)$$

Table 3-2 Blade Parameters in the Stall Model

Description	A	B	n
$F_1(c/r)$ (Snel et. al. (1993)	3	2	0
$F_1(c/r).F_2(twist+ pitch)$ (Schepers et. al. (2004)	2.93	1.178	6

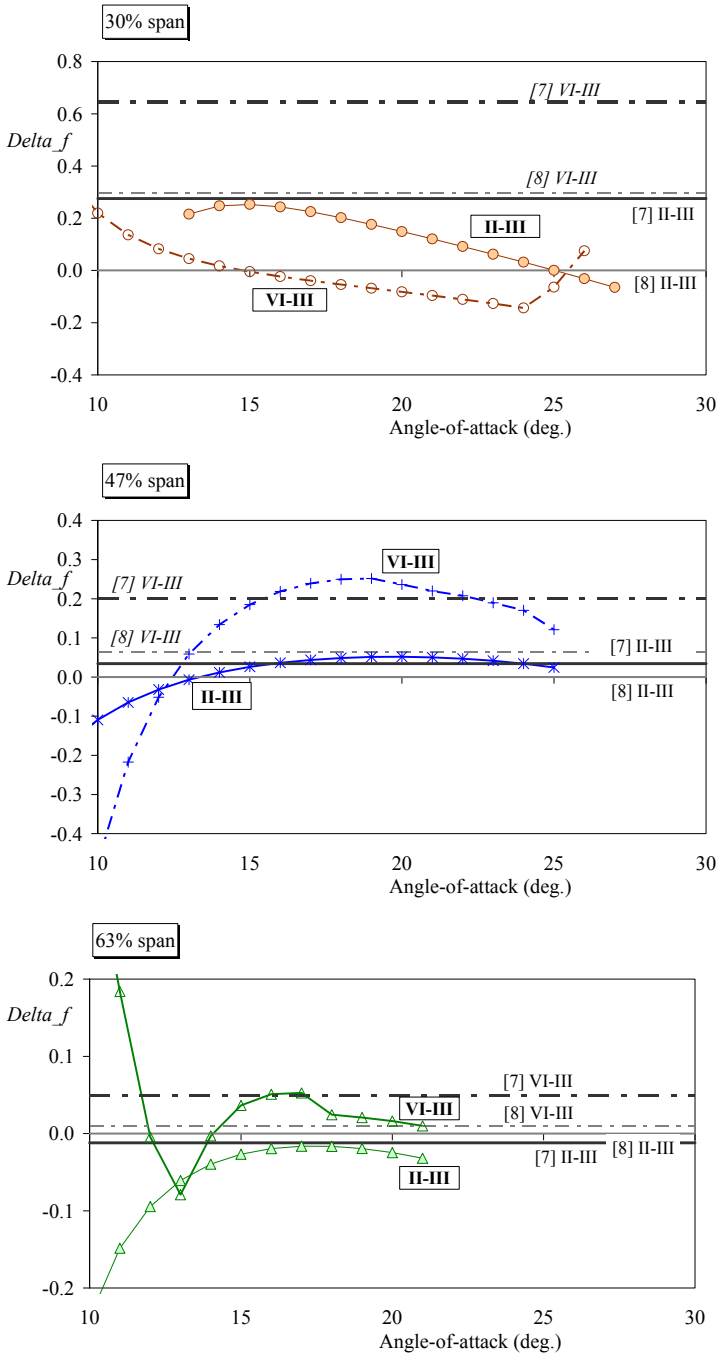

Figure 3-12 The measured difference in Delta_f compared with the result of two stall models (Table 3-2) for the NREL blades.

Two approaches are shown in Table 3-2. The model from Snel et. al. (1993), like most of the other models, does not have a relation with the blade twist and pitch angle as the model from Schepers et.al. (2004). The latter is a variation on the representation of f of Chaviaropoulos and

Hansen (2000). The stall model of Du and Selig (1999) depends basically on c/r, but the exponent is extended with a modified tip speed ratio. Its behavior for the difference in f between the several configurations is therefore comparable with Snel. The stall models of Chaviaropoulos and Hansen and Du and Selig also include a mild expression for the 3D drag and then the influence of the drag in Eq. (3) should be reexamined first.
Combining Table 3-2 and inserting the blade geometry of Table 3-1 results in constant values for f and consequently *Delta_f*. The results are given in Figure 3-12 and show the engineering model approach (given by equation 9 and 10) versus the measurement data (see example in Figure 3-11).
The largest deviation between the engineering model approach and measurements can be found at the 30% segment. It is remarkable that the measurements $_{VI}f_{-III}f$ *(=Delta_*f_{VI-III}*)* of phase VI-III lies below the other "measured" curve $_{II}f_{-III}f$ *(=Delta_*f_{II-III}*)* while the opposite is true for the engineering models.
Most interesting is that the *Delta_*f_{II-III} values from model *F(c/r)* (Snel et. al. (1993)) are always zero because the c/r values are the same for both phases and twist (+pitch) is not included (the latter term in Eq. (10) is then zero). So [8] distinguish no difference between a straight and twisted blade with the same chord distribution. The results of the measurements show however strong evidence that a twist+pitch angle dependency model is more consistent with the measurements. Except for the inboard (and tip) segments the values of *f* from (Schepers et. al. (2004) seems to be rather close to the averages of the measurements. Adjustment of the model such that the opposite trend at the 30% segment is predicted correctly, as well as keeping the good results for the other segments, can not be performed with the current description of the stall model. This contradictory outcome can not easily be achieved.
Prediction of the curved values of *Delta_f* derived from the measurements would be quite difficult with the current engineering approach. Dependency with the angle-of-attack suggests that the model possibly need to be extended with local airfoil performances.

3.2.3 CFD calculations with FLUENT

There are several numerical options to model the flow around an object eg. rotor blade. Most basic is the potential flow approach and nowadays a viscous boundary layer is added to improve the flow property description. These codes normally calculate with around a 2 dimensional model and RFOIL is an example of this. RFOIL has been extended with a radial flow description dedicated to rotational flow and therefore predictions of augmented lift due to rotation are possible. This aerodynamic code has been described in detail before and here the focus will be on the full Navier Stokes code FLUENT. These codes include a full model (!) of the flow properties in the entire domain and 3 dimensional shapes come into the research scope.
Several shape options and flow cases can be modeled and flow description is more realistic. Non-rotational or rotational flows are possible and do not need additional description of the (boundary layer) flow. Required is however a full description of the domain and defining the grid adequately is essential. Also the choice of viscosity model affects the outcome and proper investigations into such need to be part of the analysis.
The model to describe the parked configuration differs from that of the operational rotational blade configuration and here the latter will be explained in more detail.
(The configuration of the parked rotor has been presented at two conferences and can be found in *"Proceedings from the 45th AIAA Aerospace Sciences Meeting and Exhibit, Reno, Nevada, Jan. 8-11, 2007"*and *"Proceedings of the 2007 European wind energy conference and exhibition, 2007 European wind energy conference and exhibition in Milan"* and in the Journal of Solar Energy 2008, published in August 2008)

Modeling the rotational flow around the NREL blade

While only the first quarter of the upper half of the rotor plane (between azimuth angle of 0^o and 90^o) will be considered in the comparison the computational model can be limited to the blade without tower. Also neglecting the nacelle is fair because its influence is expected to be small.

The computational domain around the blade is divided in 4 blocks with an O-O topology with local mesh subdivided in 3 parts; a root, blade and tip section. The first two parts have respectively 38 cells and 99 cells in span-wise direction and 196 cells wrapped around the cross profile. The tip has 39 cells along the span and only 61 cells around the cross sections. An impression of the cell distribution at the blade surface can be seen in Figure 3-13. Construction of the blocks starts at the blade surface and to capture the thin boundary layer the height of the first inner cell is equal to 4×10-2 mm and has y+ of about one. The normal spacing has a growth rate of 1.2 and consists of 20 cells and results in the boundary layer block of 0.5×106 cells. Around this block an O-O block is wrapped around covering a 90o azimuthal area. This block contains 1.9×106 cells and the length in span-wise direction is 1.5 radius.

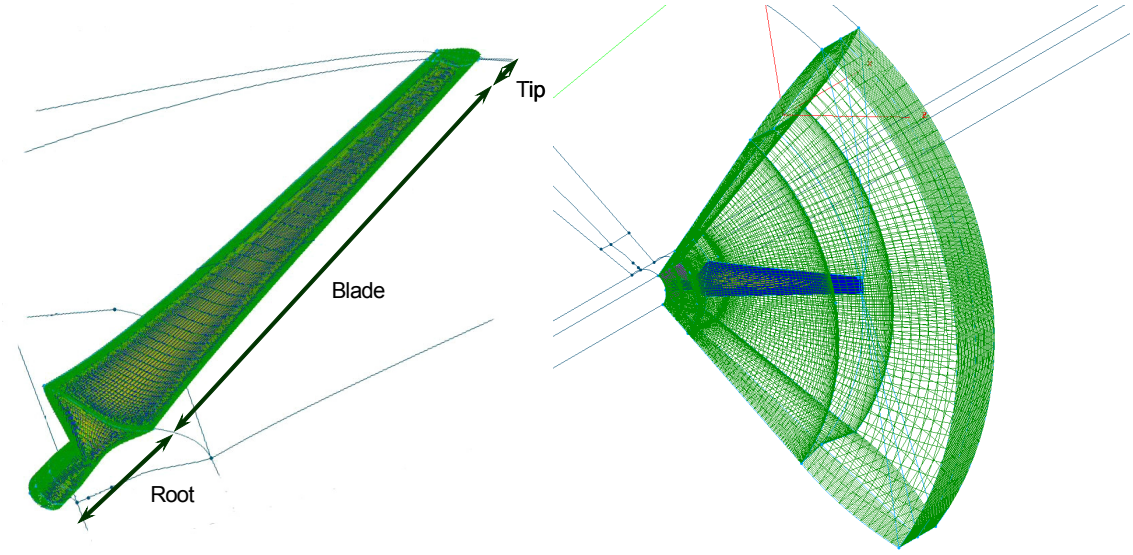

Figure 3-13 The boundary layer block (left) and the blocks immediately connected to this boundary layer block (right)

This block is surrounded by a quarter sphere with a radius of 6 blade lengths and some 0.7×106 cells. The computational domain will be completed with a fourth block covering the remaining 90◦ with 0.6×106 cells (Figure 3-14). The entire domain covers 180◦ in azimuthal direction, the up-per half of the rotor plane, and the four blocks has a total of 3.6×106 cells.

Conditions

To model the rotating blade, the blade is put at a fixed position while the fluid is given a rotational reference frame. This approach prevents the need for sliding meshes. Upstream of the spherical domain the undisturbed wind speed is specified and this is treated as velocity inlet. This is 6 blade lengths away of the blade, just like the outlet, which is a pressure outlet. At the center cylinder face slip conditions are applied, while the blade itself is modeled as a wall with no slip.

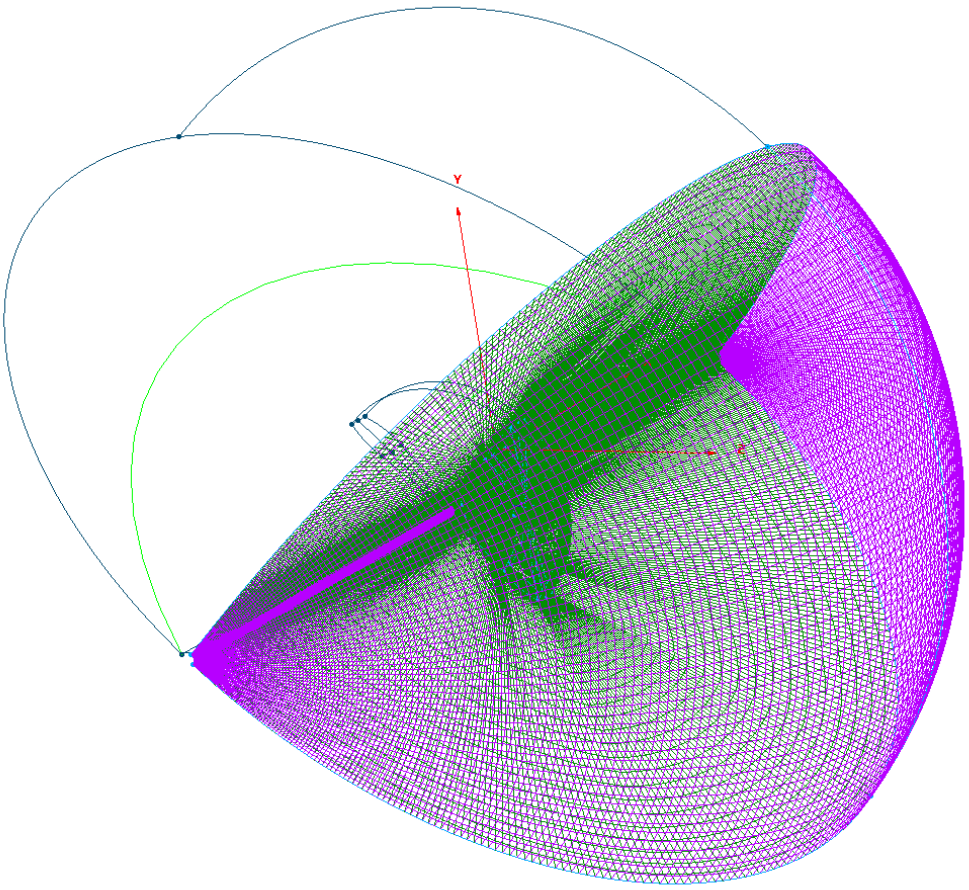

Figure 3-14 Overview of the domain with a dense spacing around the blade (block 3) and the remaining half (block 4)

Turbulence models

The investigated flow cases start with an almost fully attached flow at the lowest tunnel speed of 8m/s and with increasing wind speeds parts of the flow separate and finally result in a fully separated flow along almost the entire blade span. The flow description of partly separated flows are commonly simulated with by a k-ω SST eddy viscosity model while for huge separated areas the description of the detached eddy viscosity model, DES, is in general preferred. Here, three options will be discussed and a wind speed of 13m/s will be taken as reference.
Considered are:
1 - steady state solutions with the k-ω SST model
2 - unsteady computations with the k-ω SST model
3 - and computations with DES being unsteady.
The results at a wind speed of 13m/s are selected for detailed analysis. The unsteady models turned out to represent the measurements slightly better and a detailed analysis between the unsteady k-ω SST model and DES model is investigated.
Figure 3-15 shows the results for 4 span positions between CFD calculations and measurements. The differences between the k-ω and DES model are not that big and compared with the measurements the predictions with the k-ω model seem to be slightly better at most of the span locations. The calculations for r/R= 0.30 are not very satisfactory. This could be caused by insufficient capturing of the turbulence and/or uncertainty in the description of the shape between the calculated span location chord and the circular hub connection.

From these FLUENT results the best overall performance is obtained with the steady or unsteady k-ω SST model and this turbulence model will be used in the determination of the section characteristics up till the wind speed of 15m/s.

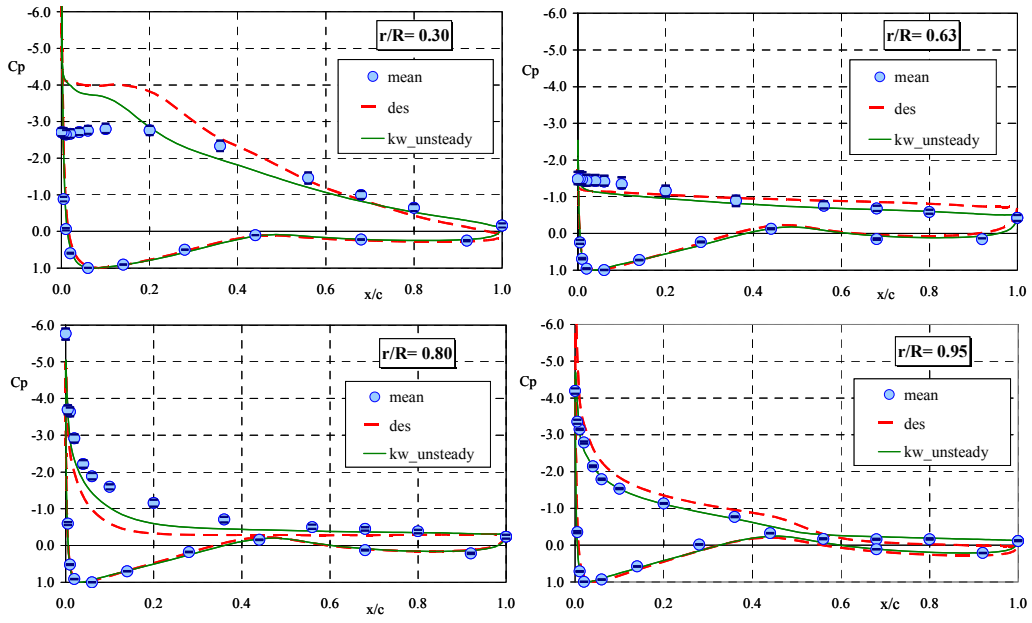

Figure 3-15 The effect of the unsteady k-ω SST and DES model on the pressure distributions compared with those of the measurements at 13m/s tunnel speed (DES is dotted line)

4. Results of research

4.1 ECN Results at non-yawed (stationary conditions)

The following conclusions have been drawn by ECN on the results at non-yawed conditions:

- Most investigated loads are predicted well with ECN's aero-elastic code PHATAS as long as the tunnel speed is relatively low (say below 10-12 m/s, which corresponds to an angle of attack below the stall angle of attack). The most pronounced exception is the overprediction of the normal force at 95% span. This is shown in Figure 4-1and Figure 4-2 which show the ratio between calculated and measured normal forces at 30% and 95% span, as function of tunnel speed for the three different pitch angles (i.e. a ratio of 1 corresponds to an optimal agreement).

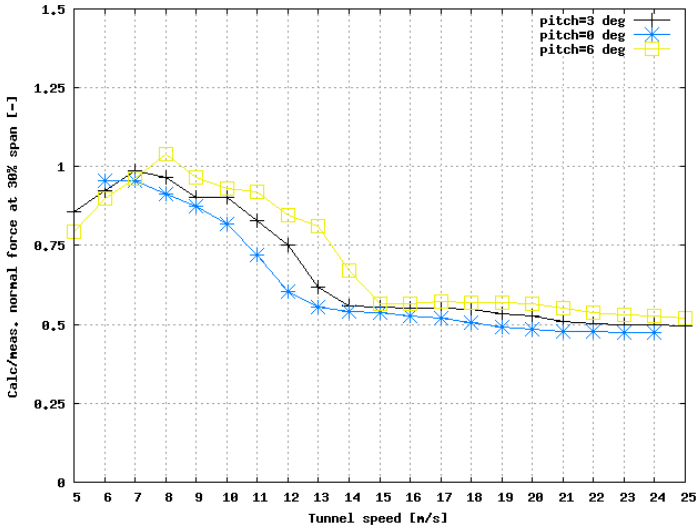

Figure 4-1 Non-yawed conditions: Ratio between calculated and measured normal force at 30% span for three different pitch angles

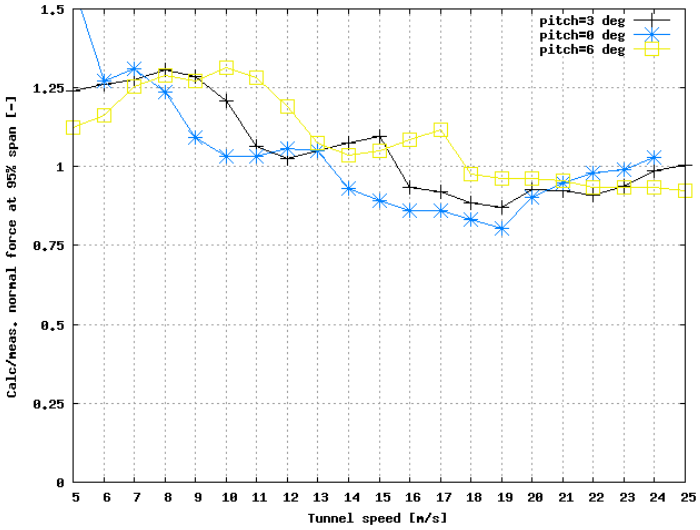

Figure 4-2 Non-yawed conditions: Ratio between calculated and measured normal force at 95% span for three different pitch angles

- At higher tunnel speeds, the PHATAS code underpredicts the normal forces and overpredicts the tangential forces. The latter observation implies the prediction of too strong a force towards the leading edge. These deficiencies are most likely caused by 3D effects in stall. It implies that the 3D correction from Snel et. al.(1993), as implemented in PHATAS, yields a too low increase in lift coefficient, where at the same time the drag should be increased. It is noted that similar observations were found in the Annexlyse project, see Schepers(2004), where field measurements on different turbines were analysed. However, the empirical corrections which have been derived from those measurements, lead for the present configuration, to an 'overcorrected' lift increase and drag increase;
- The overpredicted tangential force is reflected into an overprediction of the rotor shaft torque at the high tunnel speeds. The underpredicted normal force is reflected into an underpredicted flatwise moment;
- The calculations from the free wake lifting line code AWSM (which are only performed for low tunnel speeds) show a good agreement with the measured loads. Even at the 95% span the agreement is reasonable and better than the agreement from the corresponding PHATAS calculation. This is shown in figure 4.3. In this figure the measured normal force is compared with the normal forces predicted by PHATAS and AWSM, for a tunnel speed of 5 m/s and θ = 3 degrees.

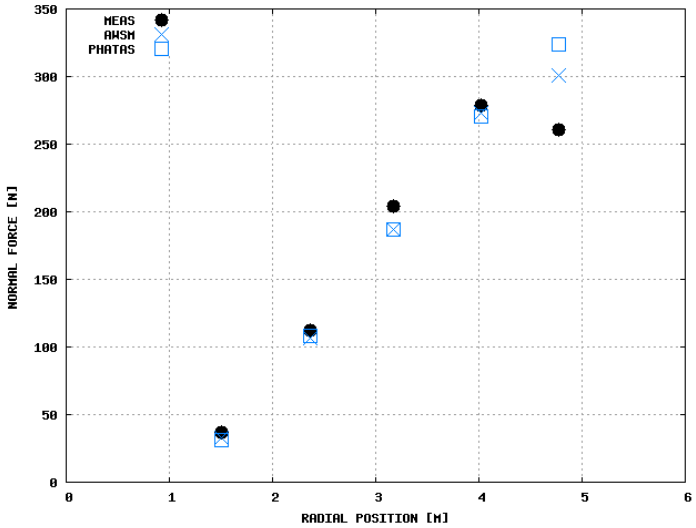

Figure 4-3 Comparison of measured normal force and normal forces calculated by AWSM and PHATAS

4.2 CFD Results parked and operating

The investigation focuses on the analysis of the airfoil segment performances along rotor blades in the parked configuration. Two wind tunnel experiments on two twisted blade geometries with different air-foils are available and were tested respectively by the Swedish Aeronautical Research Institute in the FOI LT1 low speed wind tunnel (in Stockholm, Sweden) and the American National Renewable Energy Laboratories during the non-rotating configuration in the Unsteady Aerodynamic Experiment (UAE) experiment in the NASA Ames wind tunnel (Langley, USA). The span of the blades was 2.375m and 5m, the STORK 5 WPX and the NREL Phase VI blade respectively. The lift and drag at five span locations (in-board, mid-span, outboard and tip regions) were considered and compared with the 2D characteristics. Wing model experiments up till large angles of attack with similar aspect ratio and a comparable airfoil were investigated in case of the STORK blade.

The lift at the 5 span locations are plotted as well as the data from the experiment of Ostowari and Naik in Figure 4-4. (All blade experiments were plotted with markers.) The wing models experiments were 2D and had an aspect ratio very similar to the STORK blade, A= 9.1. The airfoils and Reynolds numbers of these tests were slightly different from the FFA experiment and the most comparable configurations are used here. The inboard segment at the blade has a relative thickness of 22.5% and is larger then present in the wing models. This could explain the smaller maximum lift and different stall angle due to early turbulent separation at the upper surface. A second reason could be the influence from the inboard connection piece (which changes from airfoil to the circular attachment) giving cross flows towards inboard.

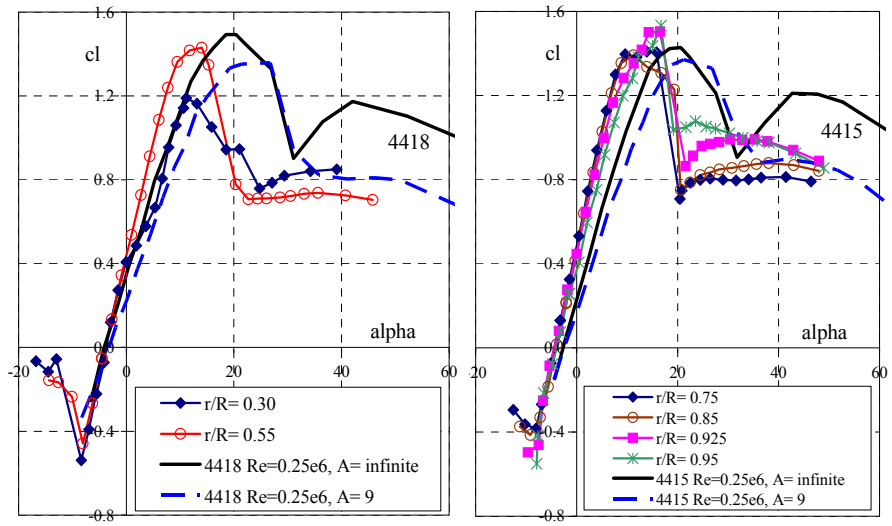

Figure 4-4 The lift characteristics from the twisted blade measurements compared to those of the straight wing model of Ostowari and Naik

The strong drop in lift at all the blade segments near 20deg. angle-of-attack in general indicates leading edge stall and this is much earlier than in the configuration of the wing models. Cross flow over the twisted blade could here be responsible. At higher inflow angles the lift curves of the segments tend to-wards the same lift values and correspond rather well with the lift curve for the full wing model.

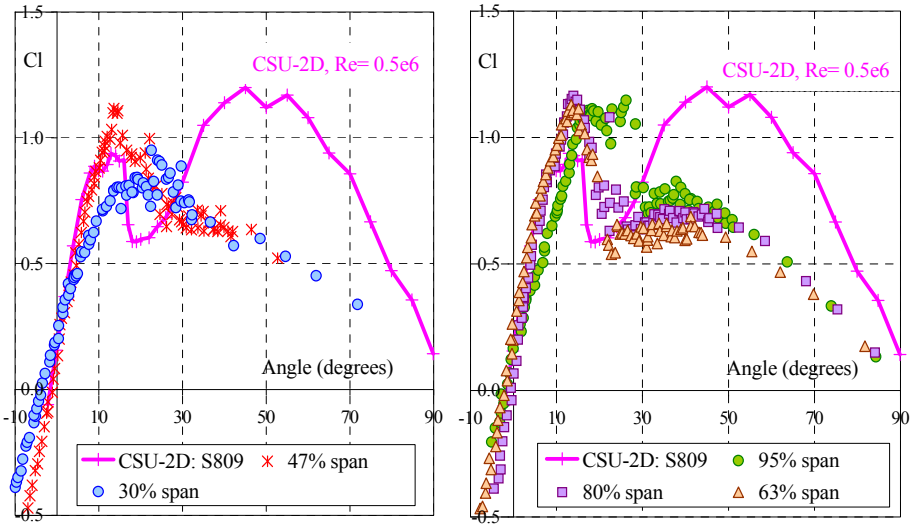

Figure 4-5 The lift curves from the blade measurements compared to 2D experimental data of CSU

In the UAE experiment every reading at 0.5deg was used and the most representative pressure distribution and accompanying normal force coefficient was selected from some 260 full readings. The inflow angle came from corrections given before and derived form the flow probe measurements. The obtained characteristics at the 5 span positions and the 2D (similar to A= infinite) results of the experiments at the Colorado State University, CSU, are plotted in Figure

4-5. Both experiments were with the same airfoil but at a different Reynolds number. This lies between Re= $1.4*10^6$ for the inboard segment and Re= $0.75*10^6$ at the tip section, while the Reynolds number in the 2D experiment is only Re= $0.5*10^6$. This complicates the comparison at small angle of attack, but is less troublesome for large angles were leading edge separation of the turbulent flow dominates. With respect to the attached flow, the linear part of the lift curve, we observe deviation at the outer ends of the blade at r/R=0.30 and r/R=0.95. This loss in lift is in general caused by the end/tip vortex and such flow conditions can be expected here. As a consequence one would expect that the maximum lift will lag behind as-well but this is only true for the inboard segment. The sharp kink in the 2D lift near 20deg. is caused by leading edge separation, and is also present at the blade segments but then less prominent. Beyond this inflow angle the difference in lift for all the blade station data are huge compared to the 2D values. However the lift differences between the several blade stations are relatively small and at larger inflow angles the lift values of the sections almost coincide. The lift in leading edge stall stays under Cl= 0.85 for all sections.

The Navier-Stokes code FLUENT was used to calculated the lift and drag at several pitch angle conditions. For that a full blade was modeled with a very dense grid distribution and the calculations were carried out wit the unsteady k-ω SST and DES turbulence model. The latter was applied for the case with huge flow separation.

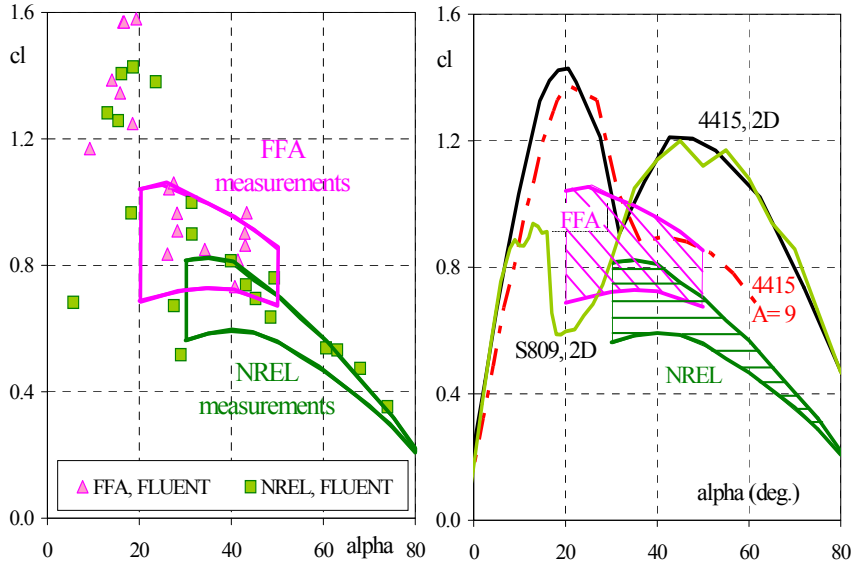

Figure 4-6 The lift characteristics of computed and measured FFA and NREL blade. The measured blade segment data are in the areas of FFA and NREL (horizontal lines)

The lift and drag values are derived from the pressure distributions and for the individual pitch angles the lift properties match reasonably well with the experiment while this was not so very good for the drag. So it is decided to focus on the overall behavior of lift and drag along the blade span. As a consequence all the acquired lift and drag data, CFD and experiments, are plotted in Figure 4-6 and Figure 4-7, respectively. The left graph of Figure 4-6 shows the scattered CFD lift values and the shaded areas which enclose the data points from the blade experiments at high angles of attack. Beyond 20deg. almost all the computed lift values for FFA (NACA 44xx series) and NREL (S809 airfoil) lies in the areas of the experimental data obtained with these blades. The trend in the lift is very similar to that of the measure-ments and reduces towards higher angles. The FAA measurements stop at lower inflow angles and lies above those of NREL. This indicates a dependency with the airfoil shape and blade layout. All span-wise measurements of the lift are well below the 2D experimental lift of the airfoils NACA 4415 and S809. These 2D curves coincide well for angles larger than 30deg. and no airfoil dependency seems to play a role here. The lower lift belonging to the smaller aspect ratio of 9, which is

comparable with that of the FFA (and NREL) blade, show a similar trend as the upper part of the FFA measurements. The tendency is downwards towards higher angles of attack but no proper comparisons with the blade segment measurements can be made beyond 50deg. angle of attack.

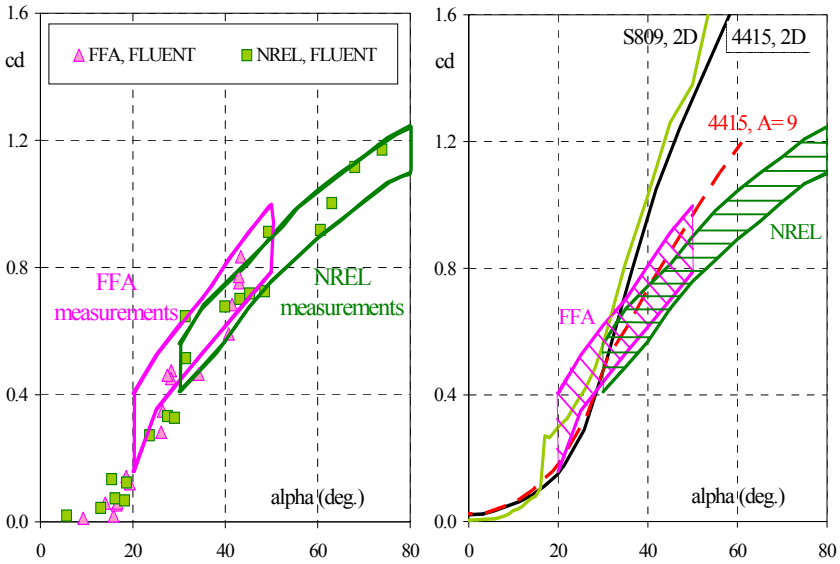

Figure 4-7 The drag performance of the computed and measured FFA and NREL blade. The measured segment data are in the areas of FFA and NREL (horizontal lines)

With respect to the drag, (almost) all computed data (beyond 35deg.) lie within the areas of the blade measurements (left graph in Figure 4-7). The area of the FFA segment measurements coincides almost completely with that of NREL. However the drag characteristics for the NREL sections continue up till 80deg. angle of attack and reaches a coefficient slightly higher than 1.2. The bandwidth of the NREL measurements is the same for the different inflow angles and similar to the FFA measurement area. Also the drag of the NACA 4415 wing model with aspect ratio of 9 stays well within the FFA area, but the mean slope of this area is different from that of the measurements on the NACA 4415 wing model and it stays unclear if that would have been the case for larger inflow angles with the FFA blade. Clear is, that the segment drag values never reach the large drag values of the 2D experiment, nor in case of NACA 44xx and S809, and the maximum drag at the segments in the parked operation will be considerably smaller than on basis of 2D measurements.

In brief, the analysis clearly shows the trends in lift and drag which could be helpful in developing tuning parameters to capture blade loads during parking conditions. Remarkable are:

- The results of the lift and drag computed with the commercial code FLUENT mostly lies within the areas of the measured segment lift and drag of the two rotor blades
- The FFA blade with NACA 44xx series show larger lift values in the fully separated flow area than the NREL blade with the S809 airfoil. The bandwidth becomes narrower with increasing inflow angle.
- The drag areas of the FFA blade and NREL blade have about the same bandwidth and coincide for a great part. The NREL blade seems to continue this trend in drag up till higher angles of attack
- The 2D experimental data are not representative for the segment performances in the parked configuration.
- The experimental results on the wing model with similar aspect ratio as the blade are reasonably close to the area with blade section lift and drag, but is does not represent individual section performances properly.

The non-yawed rotating configuration

In the sub paragraph "Modeling of the rotational flow" the method to model the flow with FLUENT is described. To achieve the best overall results the steady k-ω SST model is appropriate for the attached flow while the unsteady k-ω SST model is most dedicated to separated flows and these models will be applied here to determine the segment characteristics in the steady state non-yawed configuration between wind speeds of 8m/s and 15m/s. For these velocities the flow over the airfoil is strongly exposed to cross flows caused by rotation. This results in augmented lift and stall delay and for this part of the characteristics many engineering methods were developed. A few typical Navier-Stokes simulations will here be highlighted. The k- ω SST results in the form of span wise pressure distributions at 10m/s and 15m/s will be discussed in detail.

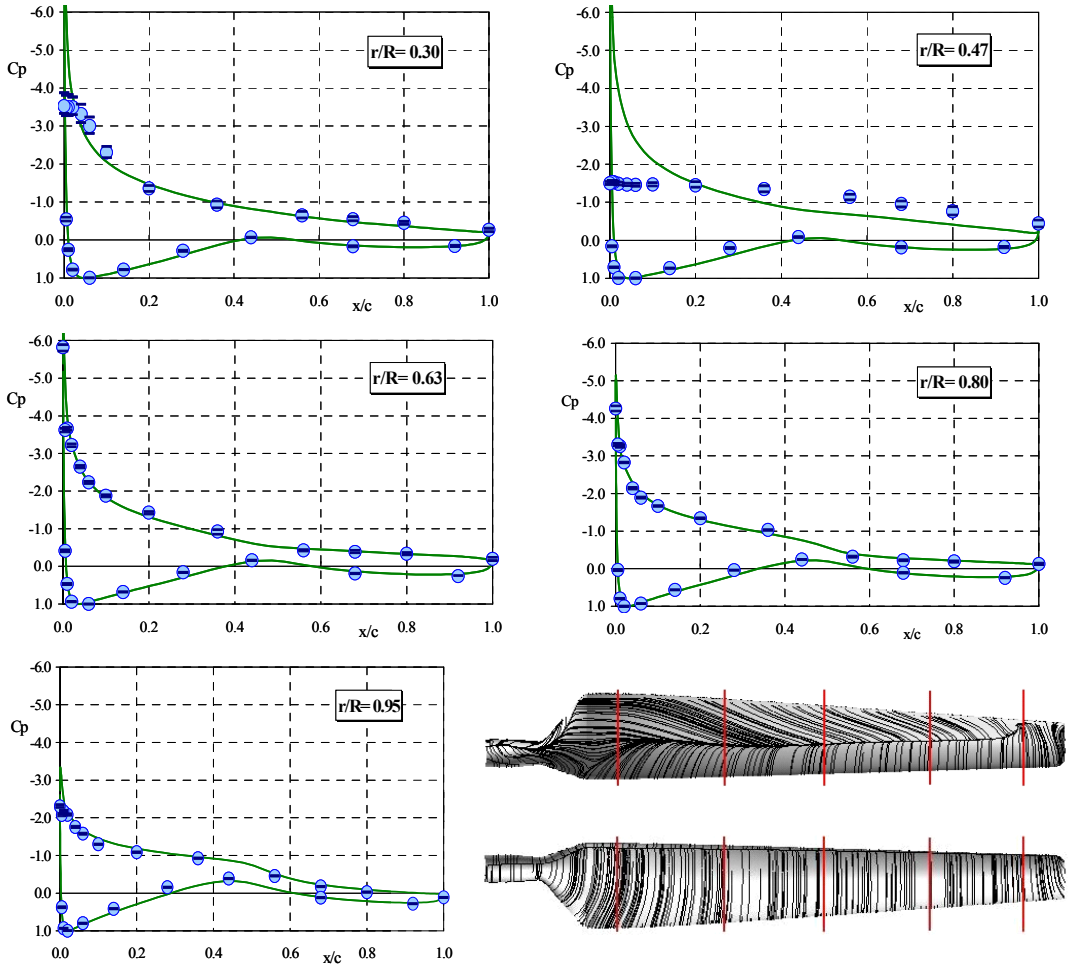

Figure 4-8 Pressure distributions for the 10m/s case plus the limited streamlines on suction (upper) and pressure side (Circles are measurements, full curve are steady k-ω SST. The error bars in the measurements represent the minimum and maximum measured Cp.)

Figure 4-8 displays the FLUENT and experimental results for 10m/s. The picture at the bottom right represents the calculated limited streamlines and shows a partly separated flow at the suction side (upper blade picture) and a fully attached flow at the pressure side. The attached flow condition can be deduced from the fact that the streamlines are aligned with the oncoming flow (which is slightly curved for a rotating blade). At the suction side CFD predicts turbulent separation at approximately 40% chord for the inboard segment and this position moves downstream to about 60% chord at the outboard part. The span segment at r/R= 0.95 however shows no turbulent separation and the flow seems to be fully attached up till the tip.

The measured values are from the UAE S-series a configuration with a clean blade without flow probes in front to minimize flow disturbances. The average data of the first rotor plane half, between 0^o and 90^o azimuth angle, is used as reference. The minimum and maximum values from the data points are given by horizontal lines and these can be observed in Figure 4-8 as-well. Only at the inboard segment, r/R= 0.30, near the nose the minimum and maximum values in the measurements are outside the markers and indicates an unsteady flow behavior and large separated flow parts are the cause of this. Normally, separated flows are reflected as a horizontal part in the pressure distributions over the back of the airfoil (in particular in 2D).

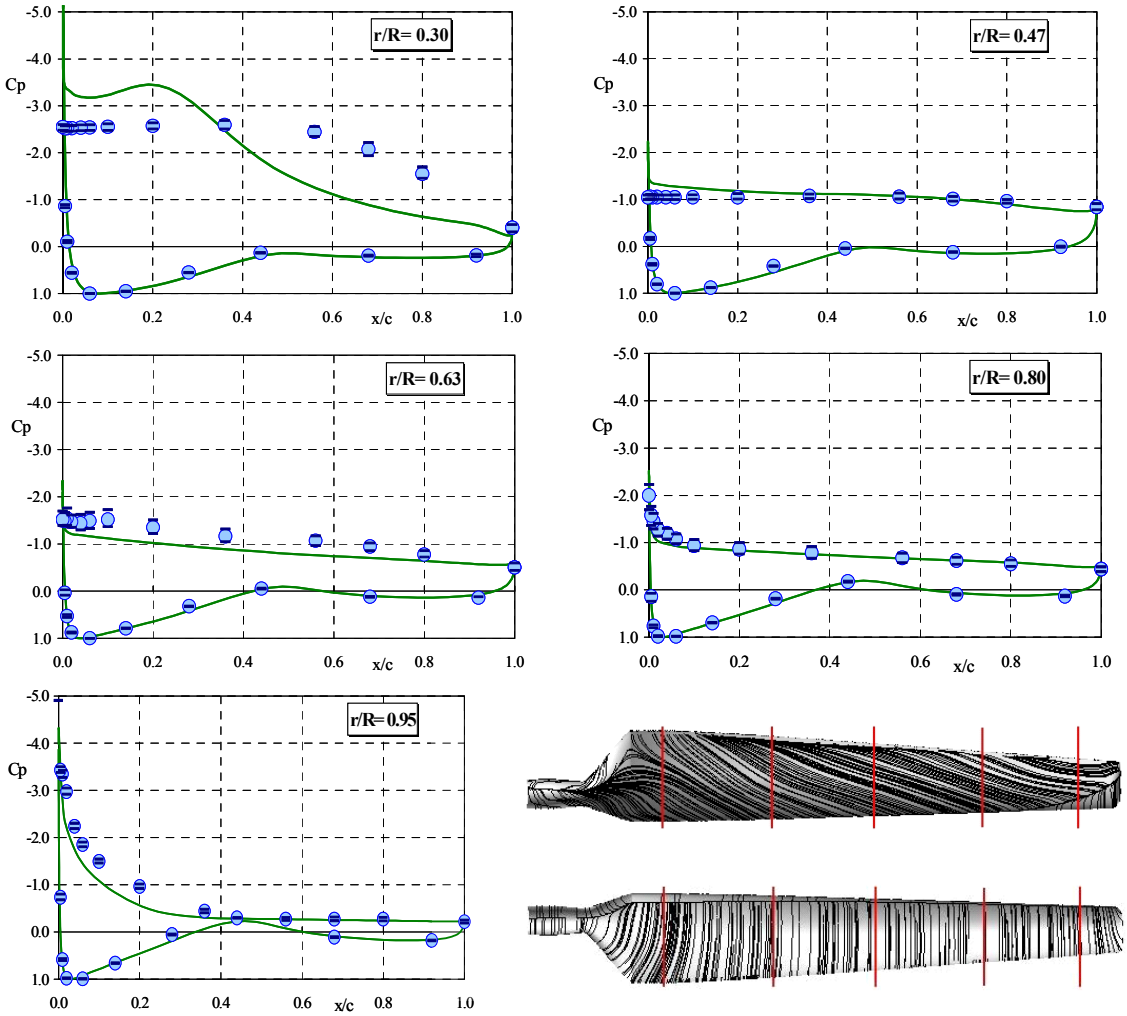

Figure 4-9 Pressure distributions for the 15m/s case plus the limited streamlines on suction (upper) and pressure side. (Circles are measurements, full curve are unsteady k-ω SST)

In the rotation cross flows have a strong effect on the separated flow and now a small pressure gradient will be present which is the true for the calculated pressure distributions as-well. Most of the FLUENT pressure distributions agree very well with the measurements, except for the r/R= 0.47 segment. Here, calculations assume a partly attached flow over the front part of the profile while the measurements represent a pressure distribution of a fully separated flow. This particular case has been studied by e.g. J. Tangler and seems to be unique. The behavior was attributed to a so called “standing” vortex, but this phenomenon is an assumption and can not be derived from a pressure distribution. The explanation came from calculations with another CFD code “EllipSys” (see next paragraph) but this behavior is different of the results with FLUENT. Towards outboard separation moves downstream and at the tip segment, r/R= 0.95, the measurements represent a pressure distribution with is comparable with an attached flow. This behavior agrees perfectly with the CFD predictions.

The pressure distributions at a wind speed of 15m/s are displayed in Figure 4-9 and this flow case is assumed to be near the top of the augmented lift due to rotation. In this figure the graph with limited streamlines indicate that four of the five segments have fully separated flows and cross flows are the dominant flow pattern at the suction side (upper picture). At the tip, r/R= 0.95, turbulent separation occurs at approximately 25% from the blade leading edge. The difference in pressure distributions between measurements and FLUENT are largest at the inboard segment at r/R= 0.30 but is in reasonable agreement at the other segments. The predictions with the unsteady k- ω SST models seem to capture the flow fairly well, what is a bit surprising for fully separated flows. This is not the case at r/R= 0.30 and the FLUENT result is very poor.
The calculated pressure distributions with fully separated flow show a very strong and small pressure peak at the nose. The increase of panels near the nose was investigated in FLUENT but the peak was hardly affected and the most likely causes are numerical errors. No change in flow pattern could be detected as-well.
The results shown here are fairly representative for the other investigated wind speeds and in general the predictions with FLUENT are surprisingly good. Two additional notes have to be made one with respect to the low wind speeds and another with the trend along the blade span. At wind speeds below 10m/s the separated flow part is small and most of the flow is attached which gives the best predictions. Beyond 10 m/s turbulent separation moves quickly towards the nose and does this faster for the inboard than outboard sections with increasing wind speeds. This is the reason why the predictions at the inboard segments are sometimes poor but the results improve towards the tip.

Characteristics
Integration of the pressure distributions along the chord gives the normal force coefficient per segment and this was carried out for the UAE experiment (S-series) and the calculations. Figure 4-10 shows the normal force coefficient versus the wind speed to get around uncertainties in inflow angle.

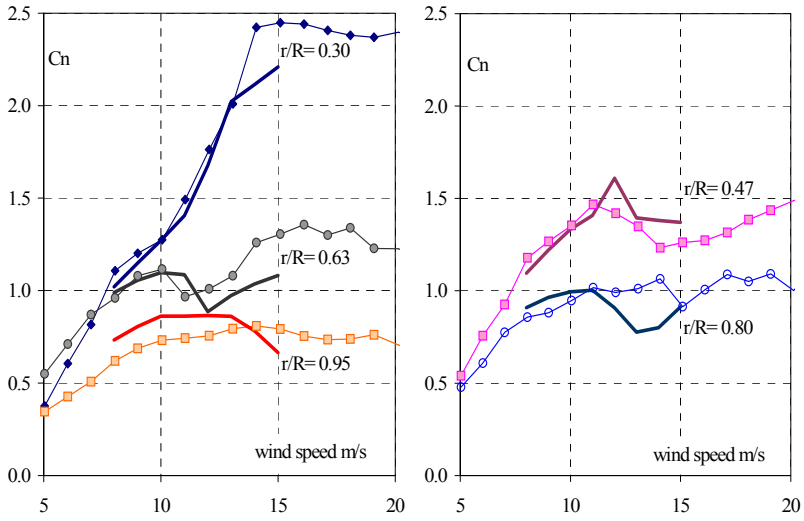

Figure 4-10 The normal force coefficient from the experiment (UAE-S series) and calculations per section (markers are measurements, full curves are k-ω SST)

The difference in C_n per segment is sometimes considerable and the inboard segment at r/R= 0.30 turns out to be the best predicted with FLUENT. This is in contrast to what was observed from the pressure distributions and differences along the chord seem to be can-celled out by the integration. Despite the differences and the sometimes conflicting results, it is clear that the trends in normal force coefficients are followed. The largest coefficients are at the inboard segments and these values reduce towards the tip. The section at r/R= 0.80 is, in general, considered close to 2D and the values at the tip are at a much lower level.

Up till 11m/s four segments are predicted very well while comparison with the tip at r/R= 0.95 is poor. At higher wind speeds deviation from the measurements become larger and this corresponds with an increase in separated flow. The relative large normal force coefficients at inboard and mid-span section will also be reflected in the lift values. To derive the lift coefficients an angle of attack is required in combination with the normal and tangential force coefficients. A proper inflow angle is not directly available and determination of it has very much to do with the definition. For convenience reasons it is decided to use the incidence from the UAE of a similar configuration as the S-series; the H-series. This approach has some uncertainties in angle-of-attack but it is expected that the effect on the CFD result will be small.

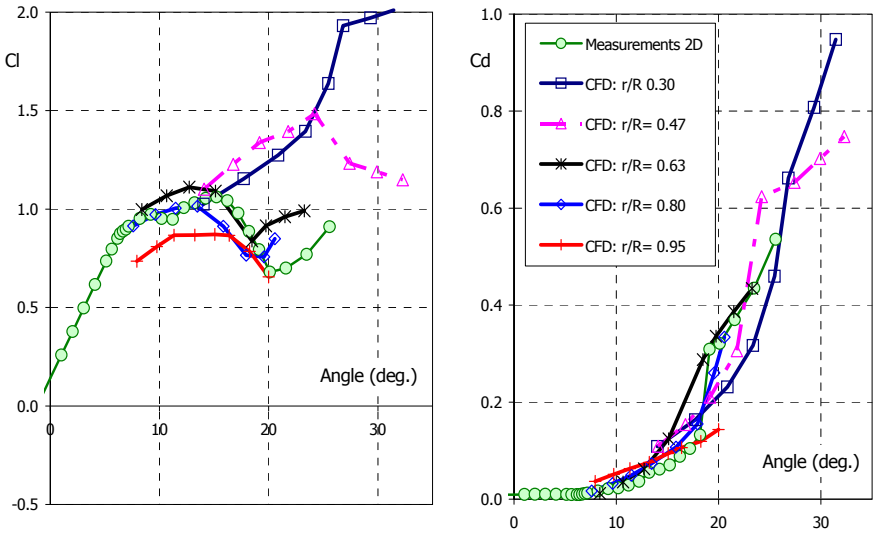

Figure 4-11 The difference between the FLUENT results due to rotation compared with the 2D S809 measurements. (The inflow angle is from the H-series of UAE)

Figure 4-11 shows the computations for the rotated blade compared with 2D measurements on the S809 air-foil. The inboard segments r/R= 0.30 and r/R= 0.47 clearly show lift levels above what is obtained in 2D and augmented lift and delayed stall is confirmed. This increase is often attributed to radial pumping of the flow in the separated area and the strong cross flows in CFD demonstrate this. The segments at r/R= 0.63 and r/R= 80 show lift curves rather close to the 2D measurements and it seems that augmented lift due to rotation is not present at this part of the blade. The tip at r/R= 0.95 show a decrease of the maximum lift and losses due to finiteness of the blade cause this.
The right graph shows the calculated drag between 15deg. and 25deg. which wind around the measured drag. This holds for all segments. The sharp rise in the calculated drag beyond 25deg. could very well lead to drag values larger then 2D measured but this can however not be establish here.
Assumptions of the inflow angle and the number of orifices at the profile nose could for instance play an important role.

In brief, the computations show good agreement for almost all segments at wind speeds below 10m/s. The biggest deviations are at segment r/R= 0.47. Beyond 10m/s large areas of the blade are separated and cross flows dominate the limited streamlines. Deviations of the pressure distributions compared with the measurements are now larger in particular at the very inboard segment at r/R= 0.30, however the results for the other segments are surprisingly good.

4.3 Engineering Models vs CFD Methods with respect to the rotational non-yawed flow

Blade loads and rotor performances of wind turbines in the rotating case can be approximated with help of engineering methods and sophisticated aerodynamic codes. The resulting segment performances can than be used to calculate blade loads and performances via Blade Element Momentum (BEM) theory or Vortex lattice like techniques

The common engineering approaches are based on 2D aerodynamic performances and results in a span-wise related adjustment. Aerodynamic methods however include at least local blade shape and (local) flow physics. A well-known program is the panel code RFOIL which has an integral boundary layer description and include a simplified cross flow model. It can be regarded as a quasi 3D code and the calculated span characteristics are still independent of neighboring segments. Full Navier-Stokes codes (or full CFD like FLUENT) include a full description of the blade geometry and the entire flow field and simulates the rotor environment properly. Aerodynamics behavior in span-wise direction are addressed directly and even nacelle layout and tower presence can be modeled.

This paragraph gives a comparison between the experimental data of the steady state NREL Phase VI blade configuration with some engineering models and aerodynamic methods.

Results

Most engineering stall models adjust the 2D airfoil characteristics for rotation and are based on the idea of Snel in which the c/r dependency plays a dominating role. They express the 3-D correction of (e.g.) the lift coefficient as a fraction of the difference in C_l between the inviscid or extended linear 2D lift. Chaviaropoulos and Hansen included twist and pitch in their base equation for the rotational characteristics and reads as:

$C_{x,3D} = C_{x,2D} + A\,(c/r)B * \cos^n(\text{twist}+\text{pitch}) * C_x$

In case x is the lift (or normal force coefficient):

$C_x = C_{l,INV} - C_{l,2D}$

or

$C_d = C_{d,2D} - C_{d,2D\text{-}min}$

$C_m = C_{m,2D} - C_{m,INV}$

The most important approaches are given by:

- Snel: A=3, B=2, n=0
- Chaviaropoulos/Hansen: A=2.2, B=1, n=4
- Schepers/van Rooij: A=2.93, B=1.18, n=6

Determination of these constants was based on (a limited amount of) measurements and therefore the applied experiments could play a rather dominant role in the value of these parameters. Figure 4-12 shows the results for the three engineering models compared with the UAE measurements for two span locations. (The normal force coefficient is chosen because then the actual integrated pressure distributions can be used and there is no relation with the (uncertain) inflow angle.) At the inboard segment the normal force coefficient extend (by definition) from the 2D measurements and strongly deviates from the 3D values (pink markers). This could be caused by the flow influences of the transition piece towards the hub which is very close to the measured segment. For the mid-span position 2 engineering methods show a huge increase in C_n compared with the measurements, while the Snel option does not show such a behavior. In general, the prediction of the maximum normal force coefficient is over-exaggerated and the methods fell short on other span positions leading to an in-proper prediction of the loads and accompanying power performances.

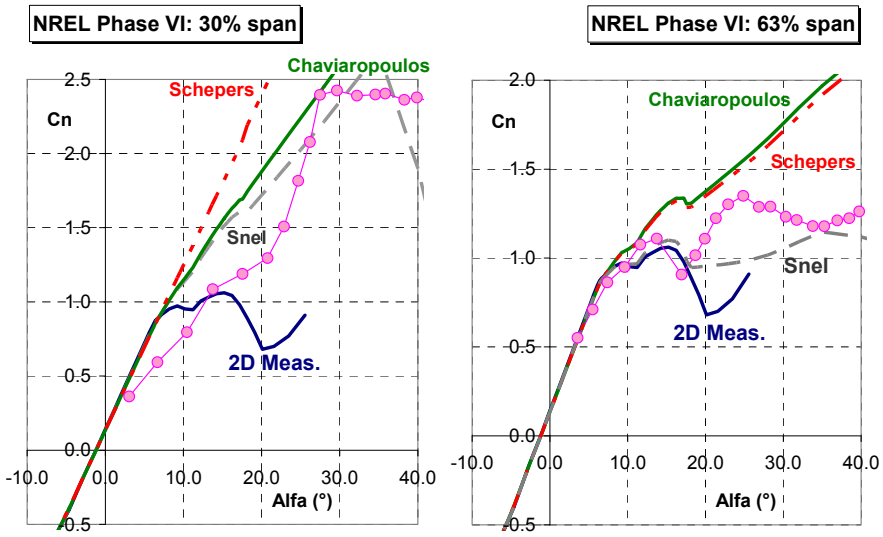

Figure 4-12 The NREL wind tunnel results for tapered and twisted blade compared with the stall model predictions for two sections (circles are UAE measurements)

The aerodynamic code RFOIL is a modification of the panel code XFOIL extended for radial flow based on the Snel-Houwink model for blade rotation. A 3-D velocity profile of Johnston was included but unfortunately this model can not handle negative velocities and separation can not be modeled adequately. To activate "rotation" the local solidity parameter c/r serves as input and 2/3 of the geometric value gives the best approximations.

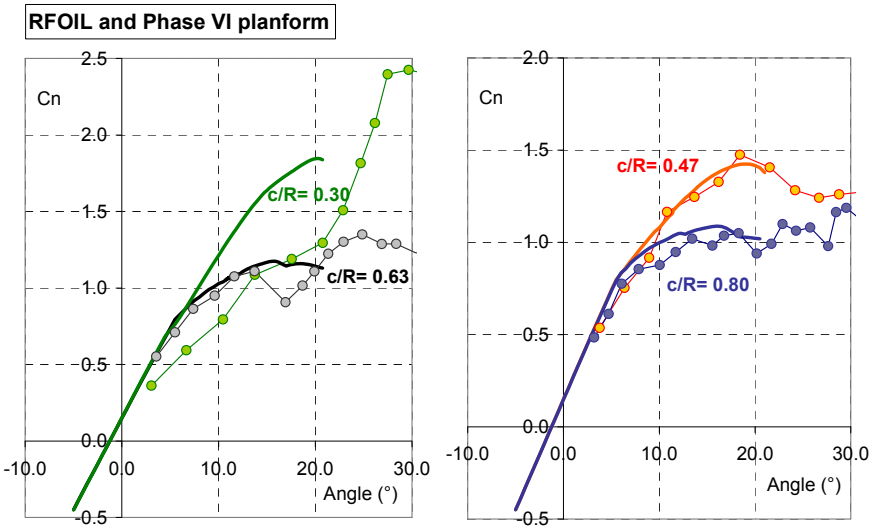

Figure 4-13 The RFOIL predictions compared with the wind tunnel results at four span sections

The results are compared with the wind tunnel measurements of NREL phase VI and are given in Figure 4-13. The normal force predictions are fairly well except for the r/R=0.30 segment, and local flow disturbances from the transition piece could obscure the measurements. The sharp nose of the S809 airfoil in combination with the integral boundary layer solution leads to convergence problems near the nose and this hampers calculation up till large angles of attack. Thicker airfoils, which are common at inboard segments, improve convergence and characteristics up till 35 deg. are in general possible.

Full Navier-Stokes codes were used to model the rotating blade. These calculations were carried out by Risø and the Delft University of Technology with respectively EllipSys3D and the commercial code FLUENT. The conditions were given by:

- EllipSys3D;
  Grid: 3.1x106 cells, domain is half sphere with radius of 6R,
  Turbulence model: fully turbulent and unsteady k-ω SST model, with max. y+ = 2
- FLUENT;
  Grid: 3.6x106 cells, domain is half sphere with radius of 6R,
  Turbulence model: fully turbulent and k-ω SST model, with max. y+ = 2.

Risø always applied the unsteady k-ω SST model, while Delft used the steady description for wind speeds below 12m/s and the unsteady k-ω SST model up till 15m/s. The differences between the steady and unsteady result turned out to be small for the range of wind speeds considered. It is than remarkable that there is such a huge difference in limited streamlines at a tunnel speed of 10m/s (Figure 4-14).

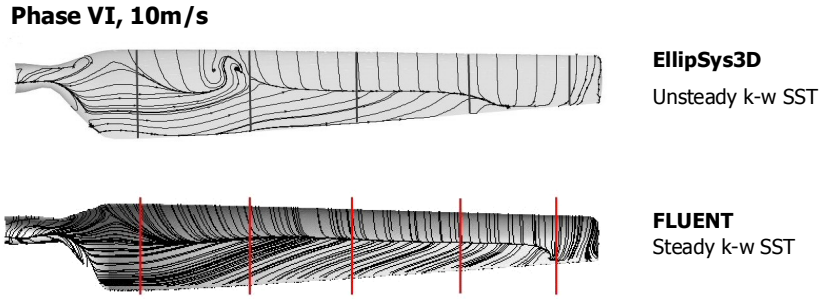

Figure 4-14 Limited streamlines on the suction side of the Phase VI blade. Vertical lines indicate the measured sections

Most interesting is the curved vortex shape nearby the 47% segment. Both front parts of the blade indicate an attached flow, and turbulent separation at the blade segment is around 50-55% in case of EllipSys3D and slightly more in front with FLUENT. This explains why the differences in normal force coefficient, derived from the pressure distributions, do not deviate much between the two codes. Comparison of the normal force coefficients for several wind speeds (10m/s, 13m/s and 15m/s respectively) along the blade span is given in Figure 4-15. Behavior and deviations in values and trends are very similar. Detailed observation of the calculated and measured pressure distributions show that integral information like C_n can be misleading because variation and deviations in pressure distributions near the nose can be cancelled out by the differences at the tail. However most of the calculated pressure distributions are quite comparable and comparison of the normal force coefficient with the measurements gives a fair indication of the quality of nowadays CFD codes.
To normal force coefficient for the five span segments is depicted in Figure 4-16. The prediction of Cn at segment, r/R=0.30, is remarkable good but also the results at segments at mid-span (r/R=0.47 and r/R=0.63) are quite surprising. The dip in the FLUENT results at 13m/s at r/R=0.80 can not be observed in the experiment and it is not clear what the cause is. The calculated outboard performance at r/R=0.95 was mostly larger then in the measurements. An explanation could be the shaping of the tip which was approximated in the CFD model.
To compare between the methods inflow angle and lift values are required. Both parameters are related to each other and uncertainties in the measured inflow angle have to be accepted. The CFD results, RFOIL and FLUENT, are compared with the experimental data in Figure 4-17 for two representative span positions.

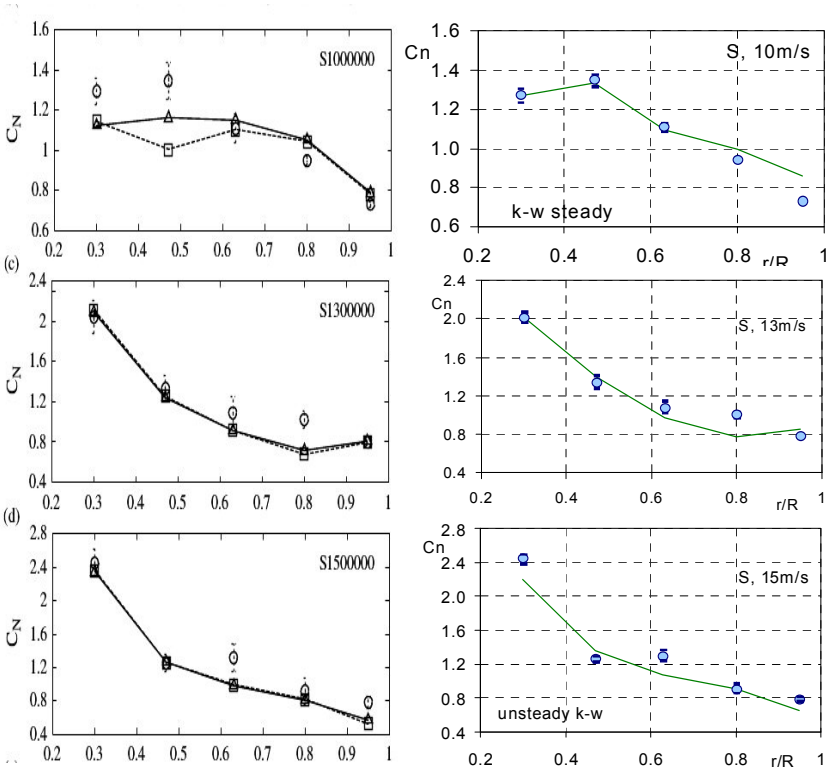

Figure 4-15 Span-wise distribution of C_n for three tunnel speeds for EllipSys3D (left) and FLUENT. Circles are the measurements while the solid line displays CFD results

As already demonstrated in Figure 4-16 the approximations of the lift with FLUENT at the r/R=0.30 segment is very well and much better then with RFOIL, and modeling of the inboard transition piece as carried out in FLUENT seems to be very important. Still the maximum lift prediction is some 20% off with FLUENT. At the 63% span location the differences are small and both CFD results seem to be quite good. The predictions of both codes at the segments r/R= 0.47 and r/R= 0.80 are comparable with results demonstrated here.

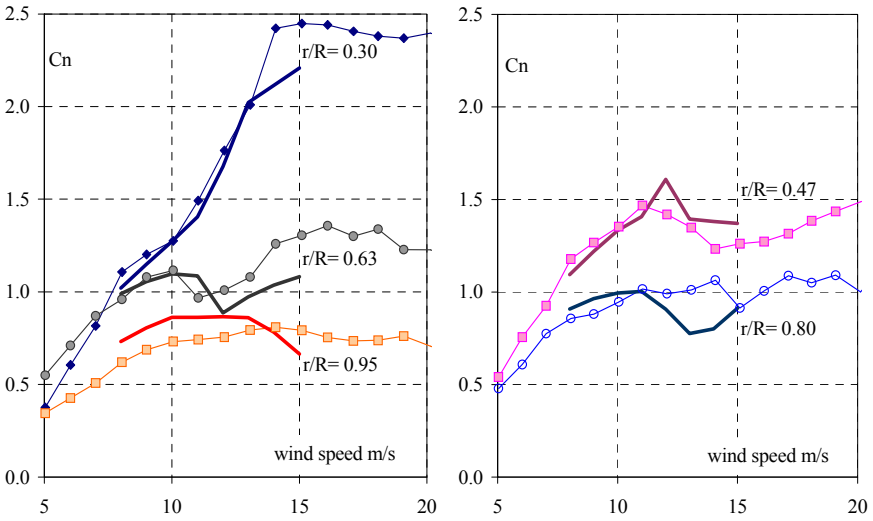

Figure 4-16 The normal force coefficients from the experiment and the full CFD results (full curves are k-ω SST model)

In brief, the comparisons of the rotational flow characteristics for the NREL Phase VI rotor blade having the S809 airfoil show that:

- Approximations of lift or normal force coefficient with help of common engineering methods are far from satisfactory. Tuning the function constants could improve the result but then the result becomes depended of the applied case,
- The results of the CFD methods, RFOIL and FLUENT (or EllipSys3D), are in general quite good and have to be preferred. The panel code RFOIL is fast but at the inboard and tip sections the influence of the transition piece or tip shape could cause large deviations. Full CFD codes do not have this drawback.

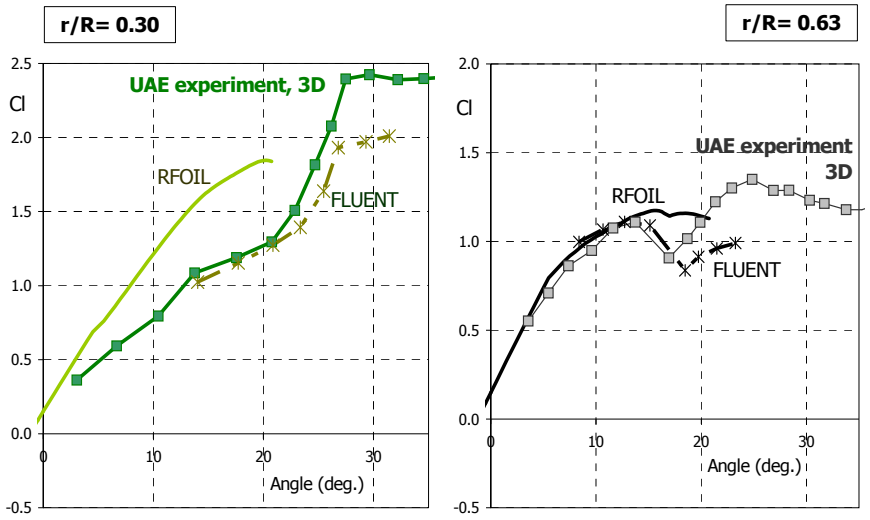

Figure 4-17 Comparison of two CFD results with the measurements

4.4 ECN Results at yawed conditions

As already mentioned before, the investigation at yawed flow put particular emphasis on the azimuthal variation of the normal forces by 1) the advancing and retreating blade effect and 2) the variation in induced velocity from the skewed wake geometry, where the latter effect is expected to be dominant at a low tunnel speed of 5 m/s and the first effect is expected to be dominant at higher tunnel speeds.

The following conclusions have been drawn from the results at a tunnel speed of 5 m/s:

- At this wind speed, the variation of the normal forces is clearly influenced by the skewed wake effect indeed, which leads to a strong radial dependency on the azimuthal variation of the normal forces. This is illustrated in Figure 4-18 and Figure 4-19 which show the measured normal force variation at the 5 instrumented sections, for the case with the highest induction (θ=0 degrees):
  - At the outboard part of the blade (Figure 4-19) the normal force varies more or less sinusoidal such that the maximum force occurs at the 'upwind' part of the rotor plane (which is between an azimuth angle of 0 degrees and 180 degrees). Such load variation leads to a stabilizing yawing moment. The variation is in line with the outcome of a conventional wake model for the calculation of induced velocities, which assumes that these velocities are induced by tip vortices only, see Schepers and Snel (1995).
  - However, at the inboard sections of the blade (Figure 4-19), the maximum value of the normal force is found to shift towards the 'downwind' side of the rotor-plane. This is consistent with previously made wind tunnel measurements of the inflow velocity, which showed the inflow velocity at the inboard station to become maximum at the downwind side of the rotor plane, see Schepers (1999). The shift can be explained by the velocities

induced by the root vortex, where conventional yaw models only consider the tip vorticity. The resulting load variation leads to a destabilizing yawing moment.

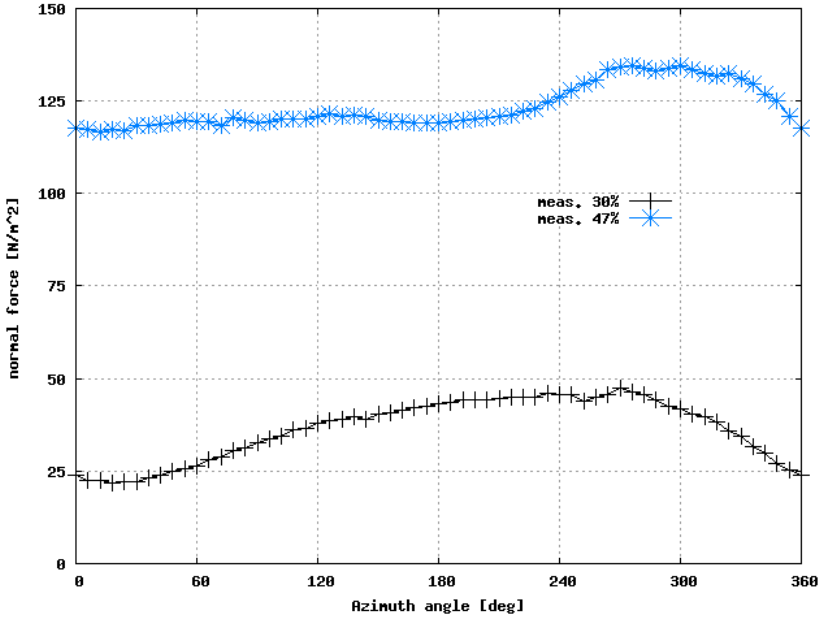

Figure 4-18 Azimuthally binned averaged normal force at V_{tun} = 5 m/s (θ=0 degrees) and a yaw angle = 30 degrees: Measured data at inner part of the blade (30% and 47% span)

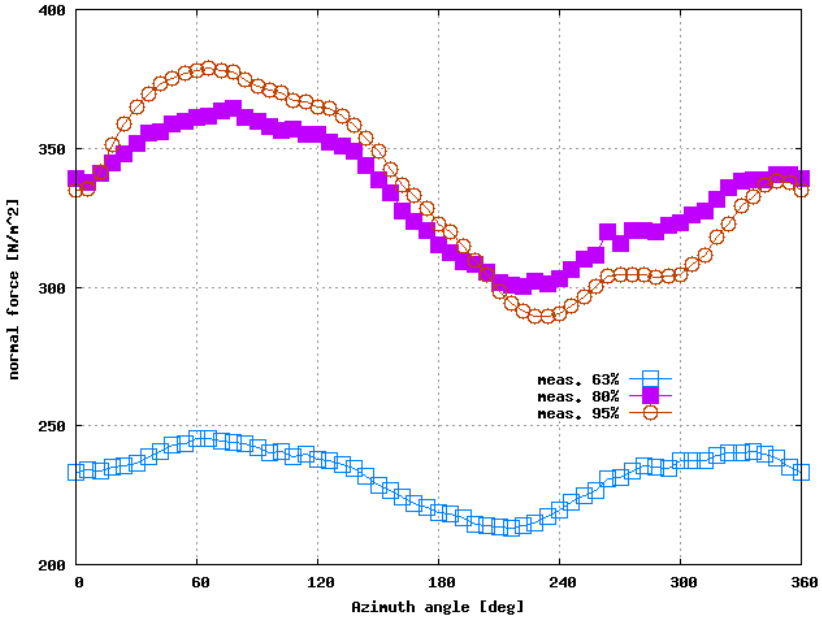

Figure 4-19 Azimuthally binned averaged normal force at V_{tun} = 5 m/s (θ=0 degrees) and a yaw angle = 30 degrees: Measured data at 63%, 80% and 95% span

- The AWSM code predicts the above mentioned radial dependency in azimuthal variation of the normal force very well. This is illustrated in Figure 4-20 and Figure 4-21, which show the normal forces at 47% and 95% span. The agreement between the AWSM results and the measurements is excellent in terms of shape of the normal force distribution (where it should be noted that the shape determines the yawing moment and that the off-set in level at 95%

span is consistent with the overpredicted normal force as discussed in section 4.1). The agreement from the PHATAS code is slightly poorer but opposite to common (engineering) yaw models, it anyhow predicts a destabilizing yawing moment near the inboard part of the blade in agreement with the measured results.

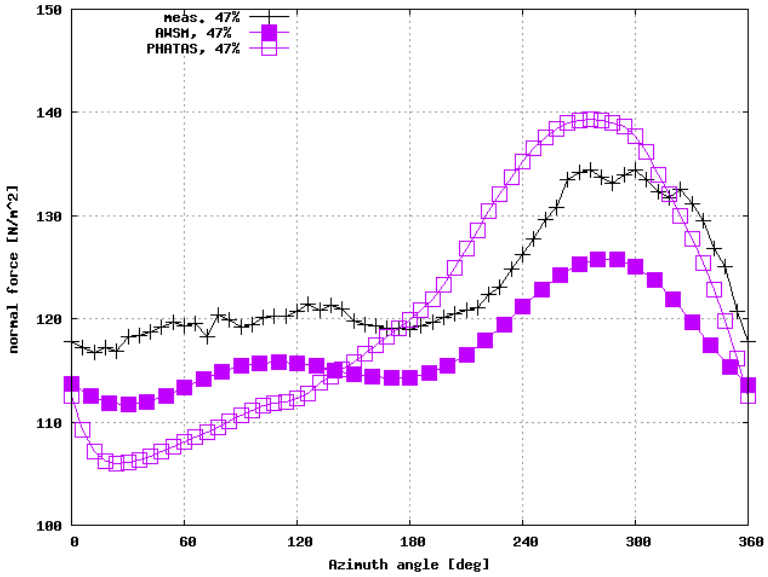

Figure 4-20 Azimuthally binned averaged normal force at 47% span at V_{tun} = 5 m/s (θ=0 degrees) and yaw angle = 30 degrees: Measured result compared with calculated results

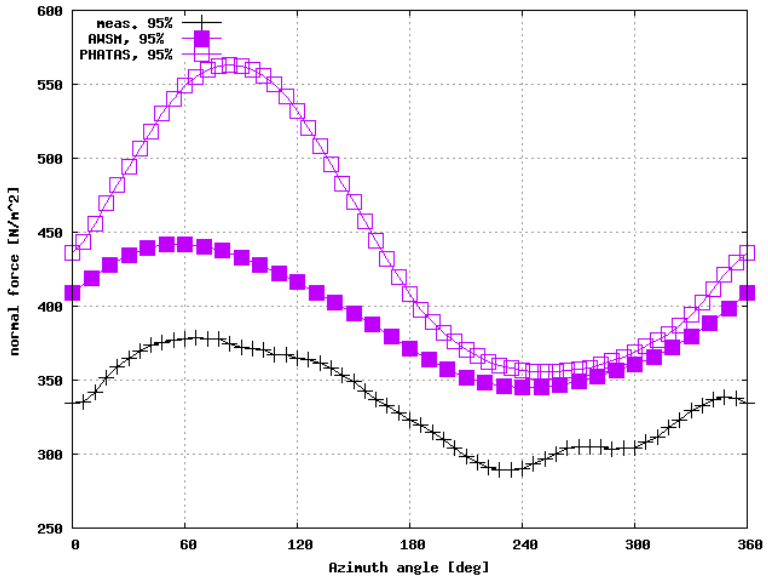

Figure 4-21 Azimuthally binned averaged normal force at 95% span at V_{tun} = 5 m/s (θ=0 degrees) and yaw angle = 30 degrees: Measured result compared with calculated results

- In order to assess the prediction of the skewed wake effect in a quantitative way, a comparison is made between the calculated and measured 'sectional yawing moments'. Thereto the $n(\theta_r)$ curves have been transformed into their contribution to the yawing moment: $M_{yaw} = -n_1(\theta_{r,1})\sin(\theta_{r,1}) - n_3(\theta r,3)\sin(\theta_{r,3})$. In this equation, index 1 denotes blade 1 and index 3 denotes blade 3. Note that the blade numbering is kept similar to the NREL blade numbering in which blade 3 is the instrumented blade. Hence $\theta r_{,1} = \theta_{r,3} + 180$. Obviously the $n_1(\theta_{r,1})$ curve has not been measured, but it is assumed to be similar to the measured $n_3(\theta_{r,3})$. The equation gives an indication whether or not the normal force distribution yields a stabilizing yawing moment contribution, since a negative value indicates a stabilizing yawing moment and a

positive value indicates a destabilizing yawing moment. The (rotor averaged) yawing moment contributions are listed in Table 4-1 (for the case with θ = 0 degrees). The results are very consistent to the qualitative observations which are given above:

- The measured yawing moment contribution is stabilizing at the outboard sections (63% to 95% span), where it is destabilizing at the inboard sections. This is also predicted by PHATAS and AWSM.
- There is a very good agreement between the AWSM calculated yawing moment and the measured values. The AWSM calculated yawing moment is generally closer to the measured values than the PHATAS calculated yawing moment.

Table 4-1 Contribution to 'sectional' yawing moment, measured and calculated by AWSM and PHATAS at V_{tun}= 5 m/s, yaw angle = 30 deg and pitch angle = 0 degrees

	$dM_{yaw,30}$	$dM_{yaw,47}$	$dM_{yaw,63}$	$dM_{yaw,80}$	$dM_{yaw,95}$
Measurements	6.9	6.3	-6.6	-24.0	-39.8
AWSM	3.9	4.7	-4.9	-27.9	-41.0
PHATAS	8.0	15.0	5.7	-34.1	-102.0

- Furthermore it is found that the induced velocities as calculated by the PHATAS and AWSM codes show, generally speaking, a good mutual agreement, even though the underlying models have very different bases.

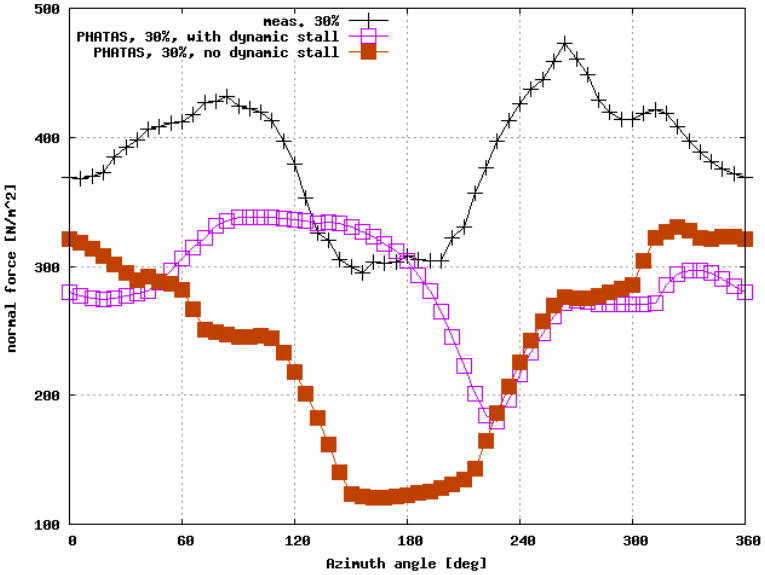

Figure 4-22 V_{tun} = 15 m/s, θ = 0 degrees and yaw angle = 30 degrees: Normal force at 30\% as function of azimuth angle: Calculated by PHATAS with and without dynamic stall

The calculated results at yawed flow and higher tunnel speeds show a much poorer agreement with the measurements see Figure 4-22. Differences occur in amplitude and phase of the normal force variation. The deviations seem to increase with angle of attack. The most likely causes for these differences are dynamic stall effects which are known to be a source for deviations between calculations and measurements. The use of a dynamic stall model leads to only a minor improvement of results. As such it is recommended to perform a more detailed analysis of dynamic stall effects. In this analysis, use can be made of measurements which have recently been taken in the Mexico project (Snel et. al., 2007). These measurements were done on a model rotor with a diameter of 4.5 meter which was placed in the German Dutch Wind Tunnel, DNW. Among others pressure measurements at a very high sampling rated (5 kHz effectively) have been taken together with measurements of the flow field around the blade.

4.5 ECN Results on dynamic inflow

The study on dynamic inflow considered fast pitching steps from -5.9 degrees to 10 degrees (i.e. an upward pitching step) and vice versa, see section 2.4 and Figure 2-9. The following conclusions have been drawn:

- At a tunnel speed of 5 m/s, strong dynamic inflow effects appear in the normal forces at all radial positions, see Figure 4-23, which shows a clear overshoot of the normal force after which the new equilibrium value is approached gradually. As explained in Snel and Schepers (1994), such behavior is typical for dynamic inflow.

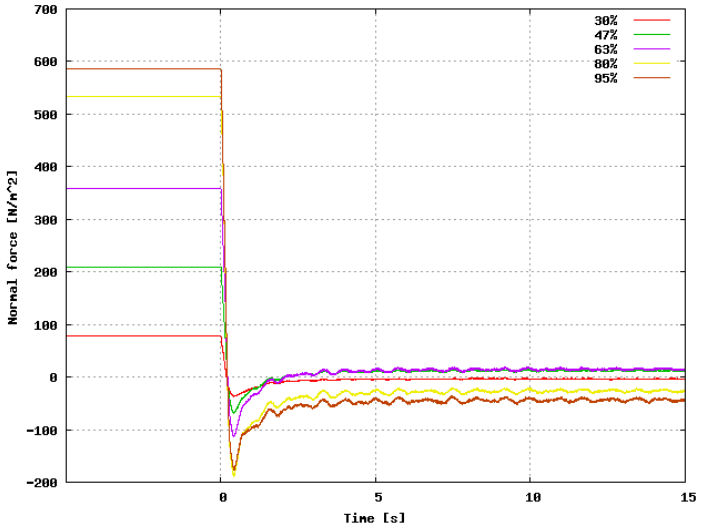

Figure 4-23 Measured normal force at 5 radial positions for the upward pitching step

- The upward pitching step is much more suitable for studying dynamic inflow effects than the downward pitching step. For the downward pitching step the angle of attack exceeds the stall angle of attack. The analysis of dynamic inflow effects is then complicated by the uncertainties which result from the stall effects;

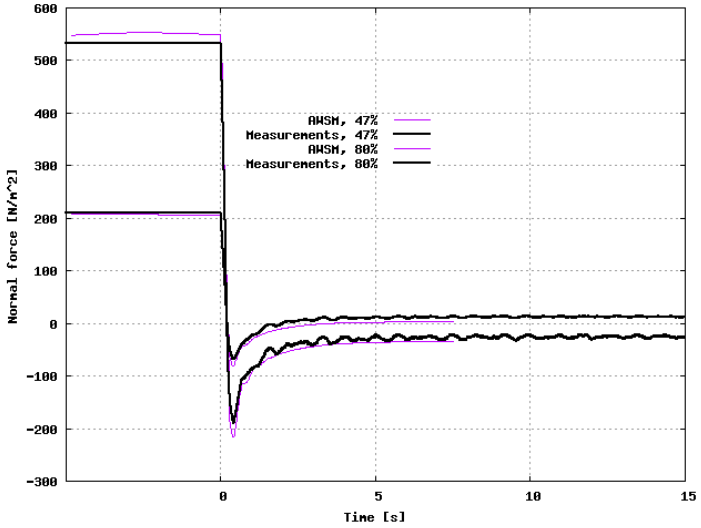

Figure 4-24 Comparison between AWSM calculated and measured dynamic inflow transient

- The agreement between the measured results and the calculated results from the newly developed free wake lifting line model AWSM (for the upward pitching step) was excellent in terms of:
  - Equilibrium values;
  - Overshoots;

- Time constant.

see Figure 4-24, which shows the comparison between the measured normal force during the upward pitching step and the normal force calculated by AWSM for the 47% and the 80% span.

- In view of the fact that dynamic inflow effects were measured at different radial positions, the present measurements allowed an assessment of the radial dependency on the dynamic inflow effect. Table 4-2 lists the time constants as derived from the measured transients in normal force, the AWSM calculated transients and from the engineering model which is implemented in PHATAS. The time constant in the measured and AWSM results, hardly reduces towards the tip. This is opposite to the expectations from previous projects on Dynamic Inflow (Snel and Schepers, 2004) and to the results from the engineering model. It is recommended to perform a similar study on the recent Mexico measurements to investigate the radial dependency of the time constant for that con-figuration. Thereafter, if necessary, the time constant in the engineering models on Dynamic Inflow need to be adjusted.

Table 4-2 Time constant for different radial positions at dynamic inflow transient

Radial position	f_{meas} [s]	f_{AWSM} [s]	$f_{engineering\ model}$ [s]
30%	0.94	1.12	0.93
47%	0.83	1.04	0.83
63%	0.76	1.04	0.68
80%	0.73	1.00	0.44
95%	0.77	1.03	0.14

4.6 Unsteady airfoil effects at attached flow

In the previous sections two different types of unsteady aerodynamic effects are discussed:
1) Induction unsteadiness, as a result of the time varying global load on the wind turbine, i.e. the Dynamic Inflow effects as discussed in section 4.5. These effects have a relatively long global time scale of O(D/U).
2) Unsteady airfoil aerodynamics in the form of dynamic stall effects, see section 4.4, the time scale of which is O($c/\Omega r$). Conceptually the first type of unsteadiness can be associated with trailing vorticity. The second type is linked to (among other items) shed vorticity. Usually the second effect is only considered at stalled conditions but there are unsteady airfoil effects present in attached flow also. These unsteady effects at attached flow do play a role in aerodynamic damping of edge wise vibrations and are now being recognized as important for stability, also for pitch controlled wind turbines, close to nominal wind speed, see Snel (2004).
Unsteady aerodynamic forces in attached flow can, in principal be accounted for by the classical model of Theodorsen (1935). This theory is basically a two-dimensional potential flow model for unsteady thin airfoils. Conceptually, the determination of unsteady forces in this theory can be divided into the following parts:

- An effective angle of attack resulting from relative motion of the airfoil with respect to an inertial system.
- An induction part, related to the time varying shed vorticity wake of the blade element.
- Solution of the Laplace equation (incompressible flow) with modified boundary conditions due to first and second bullet for the velocity field
- Determination of the pressure distribution (and resulting forces) through the unsteady form of the Bernoulli equation, containing the time derivative of the velocity potential, which is the flow inertia term.

In Theodorsen's theory, the shed vortex wake with varying vorticity is in a straight plane, emanating from the trailing edge of the section, with the vorticity vector in span wise di-rection. However for a wind turbine rotor, this conceptual picture is no longer correct. The shed vorticity will be on a helicoidal surface in the turbine wake. The situation on one blade will not only be

influenced by its own wake, but also by the shed vorticity wakes of the other rotor blades, which pass at a relatively small distance downstream of the blade in question.
Within the present project a model has been developed which treats the shed wake of all three blades by means of radial ‘spokes’. These radial vortex lines are transported into the wake by prescribed convective velocities, taking into account the average induction velocities for the steady situation, hence they are transported with a frozen wake approximation.
Unfortunately time was too short to validate the model with measurements. Since most of the IEA Wind Task XX measurements are taken at stalled conditions, the model validation anyhow re-quires measurements from another source. Thereto a future validation is planned on the Mexico measurements from Snel (2007).

5. Conclusions and future work

The measurements in the NASA-Ames tunnel as carried out by NREL gave a unique opportunity to investigate different aerodynamic aspects and to validate wind turbine design codes. Local aerodynamic quantities (pressure distributions, normal forces and tangential forces) have been obtained at different radial positions, under controlled and stationary conditions. In the present analysis ECN paid special attention to non-yawed conditions, yawed conditions and to dynamic inflow effects at fast pitching steps. The measurements at these conditions have been compared with the wind turbine design code PHATAS and the free wake lifting line code ASWM. Furthermore a new model has been developed for instationary effects at attached flow conditions.

At non-yawed conditions, the agreement between PHATAS calculations and measurements is generally good, as long as the tunnel speed is low (say < 10 m/s) although some differences appeared at the outer part of the blade (95% span). Furthermore differences appeared at high angles of attack (high tunnel speeds). Although the 3D model on the lift coefficient, as implemented in PHATAS, does improve the agreement with the measurements, this correction needs to be 'amplified'. Furthermore a correction on the drag is needed.

- At yawed conditions (and low tunnel speeds) a clear influence from the skewed wake on the induced velocity appears which in turn influences the normal force variation with azimuth angle.
- At yawed conditions and low tunnel speeds some discrepancies appear between the PHATAS results and the measurements, but opposite to common engineering models, PHATAS does predict a destabilizing yawing moment contribution at the inner part of the blade, in agreement with the measured results.
- At yawed conditions and high tunnel speeds, the agreement between the PHATAS results and the measurements is poor. The use of the dynamic stall model as implemented in PHATAS, does not improve the results.
- At fast pitching steps, clear dynamic inflow effects have been observed in terms of an over-shoot in the normal force, followed by a gradual approach towards the new equilibrium value.
- The results from the AWSM code are very similar to the results of the PHATAS code and therefore the agreement between AWSM results and the measurements can generally be considered good as well. However, at those conditions where the PHATAS code performs more poorly and where the induction is significant (e.g. at the outer part of the blade, at yawed conditions or at dynamic inflow), the agreement from the AWSM code is much better and sometimes even excellent.

Carrying out the rotor measurements in a wind tunnel reduces uncertainties at the rotor plane to almost negligible values and is a huge, very huge improvement compared to field measurements. This UAE brought a huge data base of good quality. However like other experiments some uncertainties are still there and measurements devices are often the cause. This can not be fully neglected and investigations showed that these influences are small and the given suggestions secure reliable segment characteristics. Most of fluctuations in the flow around the blade are caused by the inevitable dynamics of the experiment and defining stationary flow is then by definition impossible. The smallest variation in the segment characteristics were found in the first quarter of the rotor plane and this part should be used as reference for stationary flow. This only counts for the non-yawed flow.

Most investigations carried out by the University of Delft focus on the determination of proper rotational segment characteristics in particular for the stationary flow and determination of the correct inflow angle is of vital importance. A new method is presented to derive the inflow angle and this is in particular in the yawed flow a unique option. Prediction of the local characteristics can be carried out with help of engineering methods or via more advanced aerodynamic

codes. Including other rotor geometries like the NREL field experiments resolved that “classical” engineering methods are not well suited to predict the performances of the various segments. The best and easiest alternative seems to be the RFOIL code. Additional validation is needed in particular with respect to other airfoil profiles and wind tunnel experiments.
Future research need to include other wind tunnel experiments like the one carried out by FOI (CARDC tunnel, China) and the MEXICO partners (DNW tunnel, the Netherlands). The focus on stationary segment characteristics is needed as base but the unsteady characteristics will become more important. A more elaborate study of the many yawed cases performed in the UAE serves perfectly for these investigations. The huge UAE data base contains more interesting measurements with respect to unsteady flow like several fast pitching campaigns. Only a small part is yet studied and this counts for all partners involved in the IEA Annex 20. There are still many opportunities to research rotor flow properties from the data base and there is a long way to go before we can accurately quantify the loads on the wind turbine rotor.

As a recommendation for further work it is mentioned that the present study only considered data at the default configuration with a rotor radius of 5 m and a rotational speed of 72 rpm. However, some measurements have also been taken on an extended blade (with radius 5.5 m), and at a higher rotational speed (90 rpm). These measurements are still unexplored. The measurements at an extended blade can help to derive better tip correction models, where the measurements at a higher rotational speed may provide additional information on phenomena which are related to high induction factors.
Most of the NASA-Ames measurements were made in stall. Recently measurements have become available from the Mexico project. These measurements are taken on a 4.5 m diameter rotor placed in the German Dutch Windtunnel, DNW. Among other things absolute pressure measurements have been performed around the blade at a very high sampling rate (5kHz effectively) in combination with PIV measurements on the flow field. The measurements have been taken at stall, but also at non-stalled conditions. The Mexico measurement will provide additional insights, in particular on those effects which are not related to stall, e.g. dynamic inflow, yawed conditions, instationary airfoil aerodynamics at attached flow conditions and tip effects, but, in view of the high sampling rate, also on dynamic stall.

6. References

General:

Theodorsen, T (1935), General Theory of Aerodynamic instability and the Mechanism of Flutter. NACA Report 496, 1935.

Snel, H., Houwink, R., J. Bosschers, J. (1993), "Sectional Prediction of 3D Effects for Stalled Flow on Rotating Blades and Comparison with Measurements", *Proceedings of ECWEC,* Lübeck-Travemünde, Germany, March 1993.

Snel, H., Houwink R., and Bosschers J. (1993) Sectional prediction of lift coefficients on rotating wind turbine blades in stall, Energy Research Center of the Netherlands, ECN-C--93-052, May 1993.

Snel, H. and Schepers, J.G. (1994) JOULE1: Joint investigation of Dynamic Inflow Effects and Implementation of an Engineering Method, Energy Research Center of the Netherlands, ECN-C-94-107, December 1994.

Schepers, J.G. and Snel, H. (1995), JOULE2: Dynamic Inflow: Yawed Conditions and Partial Span Pitch, Energy Research Center of the Netherlands, ECN-C-95-056, June 1995.

Schepers, J.G. et. al. (1997),
Final report of IEA Annex XIV Field Rotor Aerodynamics Energy Research Center of the Netherlands, ECN-C-97-027, June 1997, http://www.ecn.nl/wind/other/IEA/index.en.html).

Snel H (1997) Heuristic modeling of dynamic stall characteristics In Proceedings of the EWEC 1997 Conference held at Dublin, pages 429-433, October, 1997

J.G. Schepers (1999) An engineering model for yawed conditions developed on basis of wind tunnel measurements', ASME Wind Energy Symposium, Reno USA", American Institute for Aeronautics and Astronautics", January 1999.

DU, Z., Selig, M.S., "A 3D Stall Delay Model for Horizontal Axis Wind Turbine Performance Prediction", Proceedings of ASME Wind Energy Symposium, AIAA publication, Reno, NV, USA, January-1999.

Chaviaropoulos, P.K., Hansen, M.O.L., "Investigating 3D and Rotational Effects on Wind Turbine Blades by Means of a Quasi-3D Navier Stokes Solver", Journal of Fluids Engineering, Vol 122, No.2, 2000, pp330-336.

Schepers, J.G. et. al. (2002),
Final report of IEA Annex XVIII Enhanced Field Rotor Aerodynamics Database' , Energy Research Center of the Netherlands, ECN-C-02-016, February, 2002 http://www.ecn.nl/wind/other/IEA/index.en.html).

Rooij, R.P.J.O.M. van, Timmer, W.A. (2003), "Roughness Sensitivity Considerations for Thick Rotor Blade Airfoils", J. of Solar Energy Eng. V 125, pp. 468-478, November 2003.

H. Snel, J.G. Schepers and B. Montgomerie (2007) The Mexico project (Model experiments in controlled conditions). The database and first results of data processing and interpretation

In Proceedings of EAWE, conference, 'The Science of Making Torque from the Wind', see also http://www.iop.org/EJ/toc/1742-6596/75/1.
Published in the IEA Anne XX:

Thesis (parts of this thesis focus on the NREL Unsteady Aerodynamic Experiment)
Sant T., "Improving BEM-based Aerodynamic Models in Wind Turbine Design Codes", Ph.D. Thesis, Delft University of Technology, January 2007, 451 pages. ISBN: 978-99932-0-483-1.

Journal Publications
Schepers, J.G., Feigl, L, Van Rooij, R, Bruining A (2004) Analysis of Detailed Aerodynamic Field Measurements using Results from an Aeroelastic Code, Journal of Wind Energy, Vol. 7, issue 4 pp.357-371, November 2004.

R.P.J.O.M. van Rooij and J.G. Schepers (2005) The Effect of Blade Geometry on Blade Stall Characteristics Journal of Solar Energy Engineering, November 2005, Volume 127, p. 496 – 502.

Sant T., van Kuik G.A.M. and van Bussel G.J.W. (2006), "Estimating the Angle of Attack from Blade Pressure Measurements on the NREL Phase VI Rotor using a Free-Wake Vortex Model: Axial Conditions", Wind Energy, Vol. 9, No. 6, 2006, pp. 549-577.

Sant T., van Kuik G.A.M. and van Bussel G.J.W. (2008), "Estimating the Angle of Attack from Blade Pressure Measurements on the NREL Phase VI Rotor using a Free-Wake Vortex Model: Axial Conditions", submitted to Wind Energy, under review.

Rooij, R.P.J.O.M. van (2008), "Analysis of the flow characteristics of two non-rotating rotor blades", Journal of solar energy engineering-transactions of the ASME, August 2008, under production.

Conference Publications
H. Snel (2004) Application of a modified Theodorsen model to the estimation of aerodynamic forces and aeroelastic stability, Conference proceedings of the EWEA 2004, London 22-25 November 2004.

T.G. van Engelen and E.L. van der Hooft (2004). Dynamic inflow compensation for pitch controlled wind turbines. In Proceedings EWEA conference, London, 22-25 November 2004.

Kuik, GAM van, RPJOM van Rooij, H Imamura (2004), "Analysis of the UAE phase VI wind tunnel results in the non-yawed flow", Proceedings of the 2004 European wind energy conference and exhibition, 2004 European wind energy conference and exhibition in London, November 22 - 25, 2004, EWEA, Brussel, 2004.

Rooij, RPJOM van, JG Schepers (2005), "The effect of blade geometry on the normal force distribution of a rotating blade", A collection of the 2005 ASME wind energy symposium. 2005 ASME WInd energy symposium at the 43rd AIAA aerospace sciences meeting and exhibit, January 10 - 13, 2005, ASME, New York, 2005, p. 289 – 299.

Sant T., van Kuik G.A.M. and van Bussel G.J.W. (2006), "Estimating the Angle of Attack from Blade Pressure Measurements on the NREL Phase VI Rotor in Yaw using a Free-Wake Vortex Model", Proceedings from the 25th Wind Energy Symposium and the 44th AIAA Aerospace Meeting, Reno, NV, USA, Jan. 2006.

Rooij R.P.J.O.M. van, Meng F. (2007), "Analysis of the Flow Characteristics of Several Non-Rotating Rotor Blades",AIAA-2007-625, Proceedings from the 45th AIAA Aerospace Sciences Meeting and Exhibit, Reno, Nevada, Jan. 8-11, 2007.

Meng, F., Rooij R.P.J.O.M. van (2007), "CFD Investigations with respect to Model Sensitivity for the Non-rotating Flow around the NREL Phase VI blade", Proceedings of the 2007 European wind energy conference and exhibition, 2007 European wind energy conference and exhibition in Milan, May 7-10, 2007, EWEA, Brussel, 2007.

Rooij R.P.J.O.M. van, Arens, E.A. (2007), "Analysis of the experimental and computational Flow Characteristics with respect to the augmented lift phenomenon caused by blade rotation", Journal of Physics, Conference Series, The Science of Making Torque from Wind, Lyngby, Denmark, August 28-31, 2007 (http://www.iop.org/EJ/toc/1742-6596/75/1)

IEA Annex XI/XX expert meetings
Rooij, R.P.J.O.M. van (2004), "The effect of the test set-up on the segment performance," Proceedings of the 2004 Joint meeting of IEA R&D Wind Annex XI: Joint action on the aerodynamics of wind turbines and IEA R&D Wind annex XX: HAWT aerodynamics and models from wind tunnel measurements, June 17, NREL, Montreal, 2004, p. 125 – 139.

J.G. Schepers, H. Snel and A van Garrel (2005), "Dynamic Inflow effects in NASA-Ames measurements, Radial dependency and comparison with free wake lifting line model AWSM", Presented at IEA Annex 11/20 meeting in May 2005 at CENER, Pamplona.

Rooij, RPJOM van (2005), "The effect of the test set-up on the steady state data", Proceedings of the 2005 Joint meeting of IEA R&D Wind Annex XI: Joint action on the aerodynamics of wind turbines and IEA R&D Wind annex XX: HAWT aerodynamics and models from wind tunnel measurements, Pamplona May 25 - 26, 2005, National Renewable Energy laboratory, Golden, 2005.

Rooij, R.P.J.O.M. van, Meng, F.Z. (2006), "The steady state parked configuration," Proceedings of the 2006 Joint meeting of IEA R&D Wind Annex XI: Joint action on the aerodynamics of wind turbines and IEA R&D Wind annex XX: HAWT aerodynamics and models from wind tunnel measurements, National Renewable Energy Laboratory, Golden, Colorado, USA, 2006.

Rooij, R.P.J.O.M. van (2007), "Engineering Models vs. CFD Methods with respect to augmented Lift caused by Blade Rotation", Proceedings of the 2007 Joint meeting of IEA R&D Wind Annex XI: Joint action on the aerodynamics of wind turbines and IEA R&D Wind annex XX: HAWT aerodynamics and models from wind tunnel measurements, Roskilde June 13-15, 2007, National Renewable Energy Laboratory, Golden, Colorado, USA, 2007.

Reports
Lindenburg, C. (2003) Investigation into rotor blade aerodynamics, Analysis of the stationary measurements of the UEA Phase IV rotor in the NASA-Ames wind tunnel, Energy Research Center of the Netherlands, ECN-C-03-025, June 2003.

J.G. Schepers (2007a) IEA Wind Task XX: Comparison between calculations and measurements
on a wind turbine in the NASA-Ames wind tunnel, Energy Research Center of the Netherlands, ECN-E-07-066, December 2007.

J.G. Schepers (2007b) IEA Wind Task XX: Comparison between calculations and measurements on a wind turbine in yaw in the NASA-Ames wind tunnel, Energy Research Center of the Netherlands, ECN-E-07-072, December 2007.

J.G. Schepers (2007c) IEA Wind Task XX: Dynamic Inflow effects at fast pitching steps on a wind turbine placed in the NASA-Ames wind tunnel, Energy Research Center of the Netherlands, ECN-E-07-085, December 2007.